Catena 118 (2014) 55–72

Contents lists available at ScienceDirect

Catena

journal homepage: www.elsevier.com/locate/catena

The formation of representative lateritic weathering covers in south-central Guangxi (southern China)

Wei Xiao [a,c], Ji Hongbing [a,b,*], Wang Shijie [a], Chu Huashuo [a,c], Song Changshun [a,c]

[a] State Key Laboratory of Environmental Geochemistry, Institute of Geochemistry, Chinese Academy of Sciences, Guiyang 550002, China
[b] Civil and Environmental Engineering School, University of Science and Technology Beijing, Beijing 100083, China
[c] University of the Chinese Academy of Sciences, Beijing 100049, China

ARTICLE INFO

Article history:
Received 20 April 2013
Received in revised form 9 December 2013
Accepted 27 January 2014
Available online 28 February 2014

Keywords:
Lateritic soil
The Tropic of Cancer
Mineralogy and geochemistry
Formation condition
Evolution model

ABSTRACT

The mineralogy and geochemistry have been studied in three representative lateritic weathering covers close to the Tropic of Cancer (Guangxi, South China) with the purpose of studying formation and evolution processes of lateritic covers in this region. The X-ray diffraction and scanning electron microscope analysis results indicate that the contents, particle sizes, shapes and structures of secondary minerals, such as iron and clay minerals, are distinctly different in ferruginous nodular horizon and mottled clay layer of lateritic profiles. The ferruginous nodules are characterized by high concentrations of iron and aluminum and low contents of silicon. The energy analysis suggests that there are element exchanges between hematite crystal and clay minerals. The mass balance calculation results show that there is exogenetic input of iron into lateritic covers, especially within the ferruginous nodular horizon, compared to the bottom layer of the profile. The scanning electron microscope images also confirm that voids and fractures in ferruginous nodules were filled with ferruginous material derived from soil solution. This could be a significant interpretation for the negative correlations between Fe_2O_3 and Al_2O_3. The iron and manganese oxides in ferruginous nodular horizon have an apparent effect on the adsorption and precipitation of cerium. Strontium, compared to other alkali metal and alkali-earth metal elements, concentrates in mottled clay layer. Variation in the He/Gt ratio reflected by the O/Fe ratio in a small ferruginous concretion indicates that climate changes altered aqueous activity of the soil environment. Finally, a model for the formation and evolution of typical lateritic weathering covers in south-central Guangxi, supported by all the data, was proposed.

1. Introduction

Lateritic soils (Ferralsols *sensu stricto*) are considered to be the product of weathering of basement rock under tropical climate conditions. They are rich in Fe and Al, low in silica, chemically acidic, and exhibit a soil profile different from that of other soils (Foos, 1991; McNeil, 1964; Nair et al., 2011; Tardy, 1997; Tardy and Nahon, 1985; Townsend, 1985). Laterization is a function of the soil environment which is related to the fluctuation of the atmospheric climate. The geographic latitude is the most critical of many factors that control the variation of climate. In addition, the level of CO_2 is a key factor (Berner et al., 1983) because intensive volcanic activity can induce localized high CO_2 levels, resulting in a warm and humid climate which intensifies weathering and laterization (Braun et al., 1998). Studies regarding the mineralogy, major element composition, isotopes, fluids and weathering rates have been carried out on soils developed around the Equator (Boeglin and Probst, 1998; Braun et al., 1990, 1998; Girard et al., 1997; Tardy and Nahon, 1985; West and Dumbleton, 1970; Wimpenny et al., 2007). The abundant rainfall, relatively high temperatures, intensive eluviation and generally good drainage are in favor of the development of thick lateritic weathering covers in tropical regions.

The study area is located 1° south of the Tropic of Cancer in the tropical–subtropical transition zone, with a hot and humid monsoon climate. The prominent wet and dry seasons possibly influence the groundwater levels and weathering processes. However, the typical climate in Equatorial regions is wet–tropical or tropical savanna climates which differ from the tropical monsoon climate in terms of the variation of wet and dry seasons and rainfall. The representative lateritic soil covers in our study area developed on Devonian carbonate rocks. They are characterized by a thick ferruginous nodular horizon and variegated clay layer which are similar to the *in situ* weathering of tropical soils in most Equatorial regions (Braun et al., 1990, 1998; Tardy and Nahon, 1985). Although there are many similarities in the regolith profiles there are also significant differences (Horbe and Anand, 2011; Smith, 1996). The iron nodules in the regolith have been reported as a new gibbsite-type bauxite deposit because of its high concentration of Fe and Al and low content of Si and S. The reserves of this deposit account

* Corresponding author at: State Key Laboratory of Environmental Geochemistry, Institute of Geochemistry, Chinese Academy of Sciences, Guiyang 550002, China. Tel.: +86 851 5893180.
E-mail address: hongbing_ji@163.com (H. Ji).

http://dx.doi.org/10.1016/j.catena.2014.01.019
0341-8162/

for 5% of bauxite resources in China (Liu, 1988; Wang et al., 2011; Zhao et al., 2008). The typical lateritic weathering crust is relatively well developed in the belt from Yulin to Nanning Counties. Lateritic weathering covers are best developed and concentrated in Guigang, Binyang and Hengxian Counties.

The geochemistry and mineralogy of the representative lateritic weathering crusts in south-central Guangxi have been previously studied, although they focused on the high-Fe gibbsite bauxite horizon (ferruginous nodular horizon) with respect to the metallogenic dynamics. Previous studies have shown that essential minerals in iron nodules and concretions are goethite, hematite, gibbsite and kaolinite (Chen et al., 1992, 1997; Li and Liu, 2008; Yang, 1992; Zhou and Mei, 1992). However, mineral micro-morphologies and occurrences are poorly documented. Furthermore, the relationship between iron nodules and lateritic soils, and the formation and evolution of local lateritic profiles (especially regarding the ferruginous nodular horizon) are not yet fully understood.

The purpose of this paper is to investigate the weathering mechanism and evolutionary pattern of lateritic soils. In this study, both X-ray diffraction (XRD) and inductively coupled plasma mass spectrometry (ICP-MS) were utilized to systematically study the migration and enrichment of elements. Moreover, the mineral composition was determined *via* X-ray fluorescence analysis (XRF). In order to get deeper insight into the micro-morphologies of minerals and element composition of samples, scanning electron microscope (SEM) and electron probe micro analysis (EPMA) coupled with energy diffraction spectrum (EDS) were used. Finally, a macro-scale evolution model of lateritic covers and micro-scale formation mechanism of iron nodules is established based on mineralogical and geochemical evidence.

2. Setting

2.1. Geomorphology and climate

The landforms of central Guangxi are primarily karst plains and low hills, with a mean elevation of 50 m. This differs from the mountainous region to the northwest and the coastal plains to the south of Guangxi. The capacious karst plains and hills are commonly covered by a thick weathering product that has been forming since the Tertiary. There are common, non-compacted ferruginous nodular horizons in the upper part of the weathered cover. The construction of the weathering profiles is similar to that of the lateritic profiles in the Equatorial zone described by Braun et al. (2012).

The study area is located south of the Tropic of Cancer and has a humid, tropical monsoon climate (Zhou and Mei, 1992) which is characterized by the alternation of wet (from March to August) and dry (from September to April) seasons. The AAT (average annual temperature) and AAR (average annual rainfall) are 21.5 ± 5 °C and 1580 ± 300 mm/yr, respectively. The major vegetation type is evergreen broad-leaf forest which limits the water and soil loss, and induces strong evapotranspiration.

2.2. Geology

The oldest outcrop of strata in study area is Cambrian with shale and sandstone. An angular unconformity exists between the Devonian and underlying Cambrian strata. Ordovician and Silurian strata have been denuded. Carbonate rocks are dominated lithologies of Devonian and Carboniferous that extensively distribute in study area. The Permian and Triassic successions are dominated by carbonate rocks and in conformable contact with the underlying Carboniferous strata. The Cretaceous succession is dominated by red sandstone formation that shares an angular unconformity with underlying strata. Multiphase tectonic movements and various tectonic systems led to complex sedimentary formation, folding, and jointing and faulting. Furthermore, the distribution of the Cenozoic lateritic weathering cover is distinctly controlled by the folds and faults. The Yanshanian intrusive body (Jurassic to early cretaceous), comprised of granodiorite, granite porphyry and quartz porphyry, is exposed in the study area (Zhou and Mei, 1992).

3. Sampling and analytical methods

3.1. Sampling

Three lateritic profiles in south-central Guangxi were investigated in this study; profile XY (N22°51′6.6″, E109°14′12.2″) located in the north of Hengxian County, profile LSX (N22°51′16.3″, E109°14′43.3″) was selected close to profile XY, profile WL (N23°10′59.2″, E109°1′45.7″) near Binyang County (Fig. 1).

The lateritic profiles were studied and divided according to the laterization intensity observed in the physical property, mineralogy and elemental behavior (Fig. 2). The first two study profiles are representative lateritic profiles developed on the Devonian carbonate rocks. Generally, the weathering cover in the study area consists of a thick mottled clay layer overlain by a ferruginous horizon capped by soft clayey and sandy topsoil. However, profile XY lacks the topsoil layer, probably because of intensive denudation. Profiles LSX and XY have the similar structures, so profile LSX was selected for a auxiliary study of profile XY. There is no evidence of significant input from exogenous genesis to the two profiles. However, abundant geochemical and petrographic evidence suggests that samples in different horizons show a succession and homogeneity, thus supporting observations that the weathering cover overlying the two profiles formed by *in situ* weathering and alteration of their parent rocks. Profile WL, which occurs in the Quaternary stratum, differs in that it does not contain the ferruginous nodular horizon. Furthermore, samples in this profile have lower Fe concentration, higher quartz content and a higher weathering maturity.

3.2. Analytical methods

Samples were taken from the representative horizons of each profile according to the stratigraphic order (Fig. 2). Samples were taken and preserve in zip-lock bags (*c.* 2 kg). The samples were air dried, ground in an agate mortar and sieved trough a 200 mesh (74 μm) light sieve. The major element content of bulk rock samples was determined by XRF analysis using a Philips type PW 2404 instrument. The trace element concentrations were measured by ICP-MS (Finnigan MAT Company instrument). The sensitivity of the ICP-MS is 1.0×10^8 cps (1 ppm 1n, U), and the detection limits are Fe: 20 ppt, La: 1.0 ppt and Bi: 2.0 ppt. The mineral composition was determined by XRD, and mineralogical semi-quantitative calculation was based on the lamellae spacing (d value) and X-ray relative intensity (I/I_1). The experimental apparatus was a D/max-2000 model XRD diffractometer, including the instrument standard CuKα target, with settings of 40 Kv, 20 mA, and scanning scope for 2–60°. Thin sections of soil and iron nodules with a carbon coating were observed using scanning electron microscopy (SEM-EDS) and electron probe micro analysis (EPMA-EDS), respectively. The EPMA is manufactured by the Shimadzu Corporation, Kyoto, Japan, and the EDS is a Genesis model manufactured by the EDAX Company, U.S.A. The instrument parameters were: element range from ^{5}B to ^{92}U, electron beam stability was better than 1.5×10^{-3}/H, secondary electron image resolution was 6 nm, minimum moving distance of sample set was 0.01 μm. Both the major and trace elements data were obtained from the Beijing Research Institute of Uranium Geology and the other measurements were carried out at the Institute of Geochemistry, Chinese Academy of Sciences.

3.3. Mass balance calculation

In order to investigate the transportation and enrichment of major and trace elements during weathering and pedogenesis, a method of

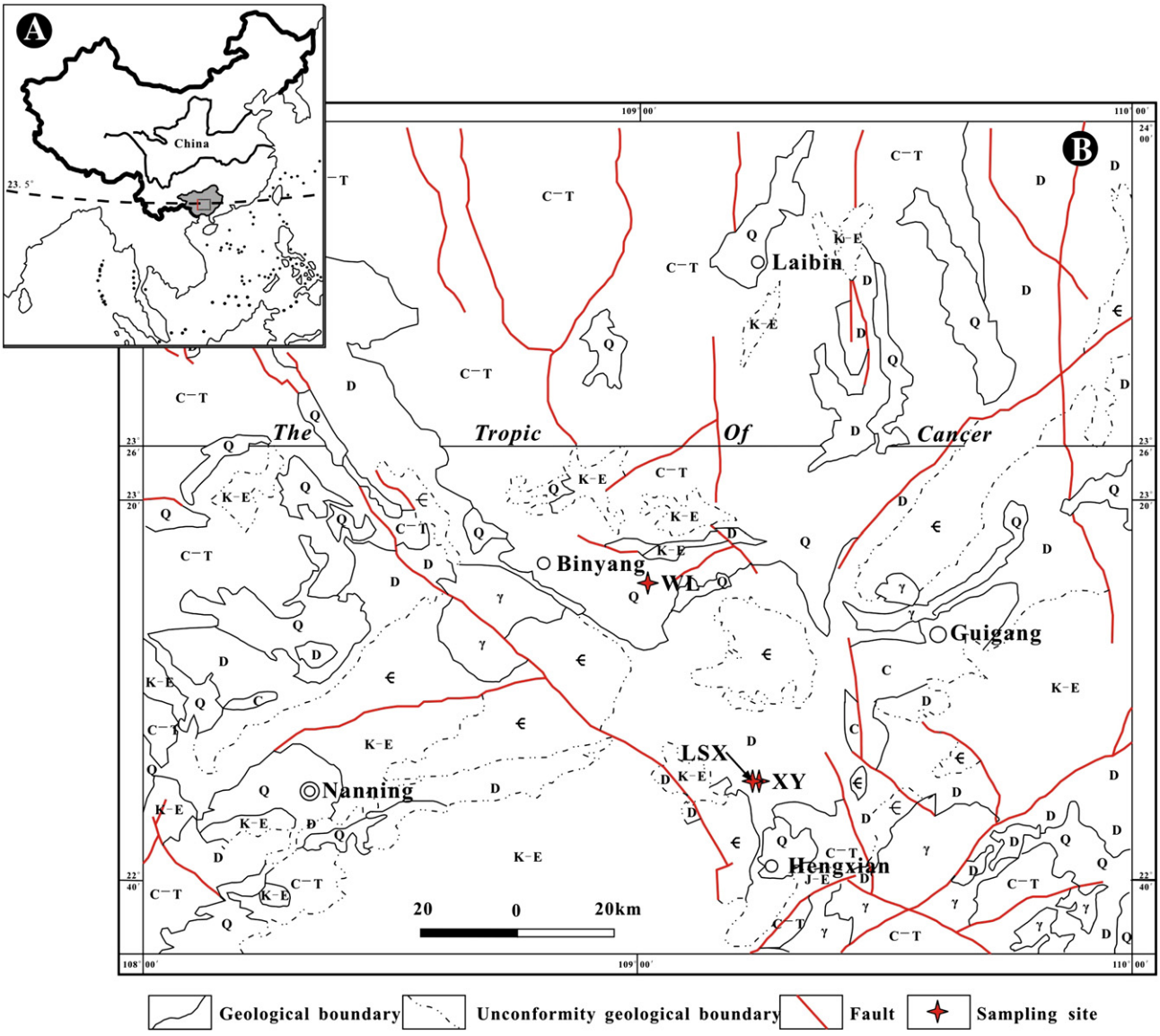

Fig. 1. (A) Location Guangxi within P.R. China and (B) a map of the study area illustrating sampling sites, stratigraphic and structural characteristics. (Q—Quaternary, K–E: Cretaceous–Tertiary, C–T: Carboniferous–Triassic, D—Devonian, —Cambrian, γ—intrusive body).

mass transport calculation was proposed (Brimhall and Dietrich, 1987; Mancktelow, 1994). Subsequently, many similar approaches were presented, such as mass change calculation (Calagari and Abedini, 2007; Maclean, 1990), enrichment factor (Zoller et al., 1974), % change in ratio (Nesbitt and Markovics, 1997), mobility index (Ng et al., 2001) and mass balance calculation (Beauvais and Colin, 1993; Feng, 2010). In this study, the mass balance calculation method was selected to investigate the behavior of various elements in representative lateritic weathering cover in south-central Guangxi. The element Zr was determined to be the immobile element profile in profiles XY and LSX *via* the "immobile plateau" method (Gong et al., 2011). According to the mass balance calculation, the transportation and enrichment of any element X in a sample relative to the fresh parent rock can be expressed by the mass transfer coefficient, τ. The coefficient τ is defined by the Eq. (1) (Chadwick et al., 1990; Nesbitt, 1979).

$$\tau = (X/Zr)_S/(X/Zr)_P - 1 \quad (1)$$

where S refers to any sample and P represents the fresh parent rock. If $\tau = 0$ then the element X in a sample has no mobility related to the fresh parent rock. However, if $\tau > 0$ it denotes the external addition of element X. If $\tau < 0$, the element X in a sample is lost during weathering, and $\tau = -1$ means X is completely removed. In this study, the fresh parent rock is replaced by the bottom layer of profile XY (sample XY-1) for calculation, because it cannot be confirmed that the bedrock is the parent rock of the weathering profiles. Here the mass transfer coefficient τ represents the mobility of the element X in a sample related to the bottom of the mottled clay layer (sample XY-1).

4. Results

4.1. Mineralogical composition

The XRD pattern and mineralogical semi-quantitative calculation of selected representative samples for profiles WL and XY are plotted in Fig. 3A and B. The XRD results show that the two profiles have significant differences in mineral compositions and concentrations. For example, the major mineral compositions of profile WL are: quartz + clay minerals (mainly kaolinite) + gibbsite, whereas the main assemblage in profile XY is: clay minerals (mainly illite, smectite and kaolinte) + quartz + gibbsite + goethite + hematite (Fig. 3).

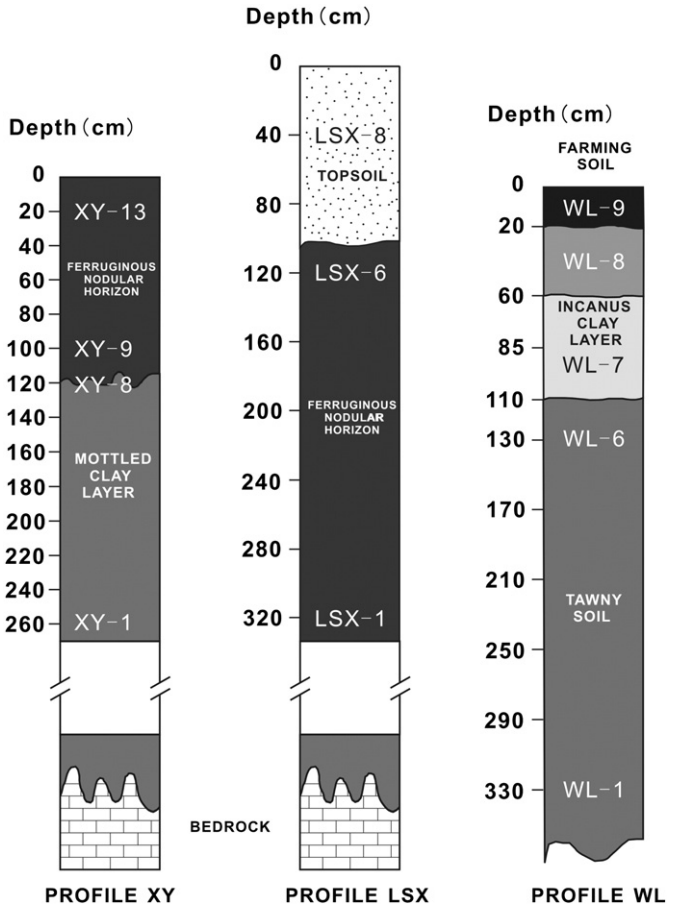

Fig. 2. Schematic representation of studied weathering profiles showing the sectional structure and sampling depth.

There is a obvious variation of mineral composition and content from the bottom to the top of profile XY. For example, from the mottled clay layer (sample XY-1) to the upper part of mottled clay layer (sample XY-7), and then to the ferruginous nodular horizon (sample XY-11), the illite (49.24% → 45.49% → 4.25%) and quartz (25.12% → 17.86% → 14.25%) show an evident decrease. However, the content of kaolinite (4.16% → 9.15% → 14.62%), gibbsite (trace amount → 2.16% → 16.18%) and goethite + hematite (6.21% → 14.24% → 34.81%) increase progressively in the same profile (Fig. 3B). In profile WL, from the bottom to top (sample WL-1 → WL-4 → WL-7), quartz displays a decreasing trend (76.48% → 48.71% → 11.66%), whereas the content of gibbsite (13.20% → 26.18% → 58.65%) and kaolinite (7.18% → 10.62% → 19.65%) increase.

4.2. Morphological features of major minerals

Grains of quartz with clay mineral coverings have a variety of particle sizes and have developed fractures (Fig. 4A and B). Zircon crystals are less fractured and cleaved than quartz (Fig. 4B). Although a small amount of ilmenite was observed by EPMA-EDS, anatase is the main Ti-bearing mineral in lateritic weathered crusts. Fine-grained anatase is widely scattered within the clay mineral matrix, and larger grains usually have fragmented edges (Fig. 4C). Overall, it is evident that quartz, anatase and zircon are the major weathering-resistant minerals in lateritic covers in the study region as observed elsewhere (Buggle et al., 2011; Cornell, 1993; Nesbitt and Markovics, 1997; Papoulis and Kalampounias, 2008; Papoulis et al., 2009; Schaetzl et al., 2006). Gibbsite mainly occurs in the form of fine grains or crystals with various sizes (commonly range from 1 to 10 μm) and amorphous shapes in soil or clay (Fig. 4D). Gibbsite mainly coexists with Fe oxides and hydroxides in iron nodules, filling the void spaces and thus forming a matrix (Fig. 4J). Kaolinite occurs as earthy or massive cryptocrystalline aggregates (Fig. 4A), and illite presents a micro-squama texture in SEM images (Fig. 4G). Hematite and goethite existed within clay minerals in amorphous and crystalline states (Fig. 4E–H). Abundant fine hematite grains are concentrated together and form large aggregates which have a spongy appearance in the clay matrix (Fig. 4E and F). In iron nodules, however, hematite and goethite are assembled together and form ferruginous ooides and concretions cemented by kaolinite or ferruginous materials. The iron nodules also contain various voids and fractures, and many of them were filled with ferruginous material derived either partially or completely from a soil solution (Fig. 4I and J).

The EPMA-EDS analysis shows that a portion of the primary detrital biotite altered to vermiculite, retaining the original shape of biotite, by cation exchange of K and Mg (Fig. 5A and B) (Banfield and Eggleton, 1990; Kretzschmar et al., 1997; Lucke et al., 2012; Nesbitt and Markovics, 1997). Monazite also occurs, and has a rounded shape and the highest reflectance in EMPA images. Monazite contains abundant P, Th and light rare earth elements (LREE) (Fig. 5C and D).

4.3. Chemical composition

The whole rock geochemical data including major, trace and REE, along with other relevant parameters for lateritic weathering covers are displayed in Tables 1 and 2. The depth variation of CIA (Chemical Index of Alteration) (Nesbitt and Young, 1982) for the three profiles had been calculated and plotted in Fig. 6A. Samples in the mottled clay layer of profile XY have similar, and relatively low, CIA values (<85). The CIA value increases progressively in the ferruginous nodular horizon (>90). The CIA value in the topsoil of profile LSX, however, is lower than that of ferruginous nodular horizon, which implies that the topsoil layer possibly did not form as an *in situ* weathering remnant. Profile WL has a high weathered maturity (CIA >97) and CIA values do not vary greatly. Moreover, at 85 cm depth (corresponding to sample WL-7) the highest CIA value is encountered (Fig. 6A). There is an obvious positive correlation between the Al_2O_3/SiO_2 ratio and CIA in profile XY and LSX ($R^2 = 0.93$ and 0.88, respectively) (Fig. 6B). Meanwhile, Al2O3/SiO2 ratio in ferruginous nodular horizon is higher than that in mottled clay layer. In the case of Fe_2O_3 *versus* CIA (Fig. 6C), there is a positive correlation within profiles XY and LSX ($R^2 = 0.86$ and 0.74, respectively), whereas no such correlation is observed for profile WL. The significant correlation between CIA and major element content and ratios indicates that weathering maturity is a critical factor in controlling element distribution.

Fig. 7 displays depth profiles with respect to selected elements: redox sensitive (V, Cr, Fe, Mn), potentially immobile (Th, Zr, Nb, Hf, Ti), potentially mobile (Na, K, Rb, Ca, Mg, Sr, Ba), Al, Si, P, U and heavy metals (Co, Cu, Zn, Ni) (Braun et al., 2012). For profile XY, the first key observation is that both major and trace element concentrations in the mottled clay layer do not vary significantly with increasing depth, whereas those in the ferruginous nodular horizon show striking changes with depth. This is consistent with the distribution of CIA which has distinct values from the Earth's surface to a depth of 120 cm, with no evident variation beneath this depth (Fig. 6A). There is strong depletion of K, Rb and Ba in the ferruginous nodular horizon compared with the mottled clay layer. However, the other alkali and alkali earth elements, such as Na and Mg, show a slight depletion. Concentrations of these elements, along with Al and Si increase progressively with an increase in sampling depth. Siderophile elements such as Fe, Mn, V, Cr, Co, Ni, Cu and Zn, along with U, show an enrichment trend in the ferruginous nodular horizon, with the highest concentrations at a depth of 80 cm. The elements Th, Zr, Nb, Hf and Ti do not vary throughout the profile except for a slight enrichment in the ferruginous nodular horizon. The element distribution pattern in profile LXS is similar to that in profile XY. The topsoil layer has a lower CIA value, higher content of alkali and alkali earth elements and lower concentrations of siderophile elements

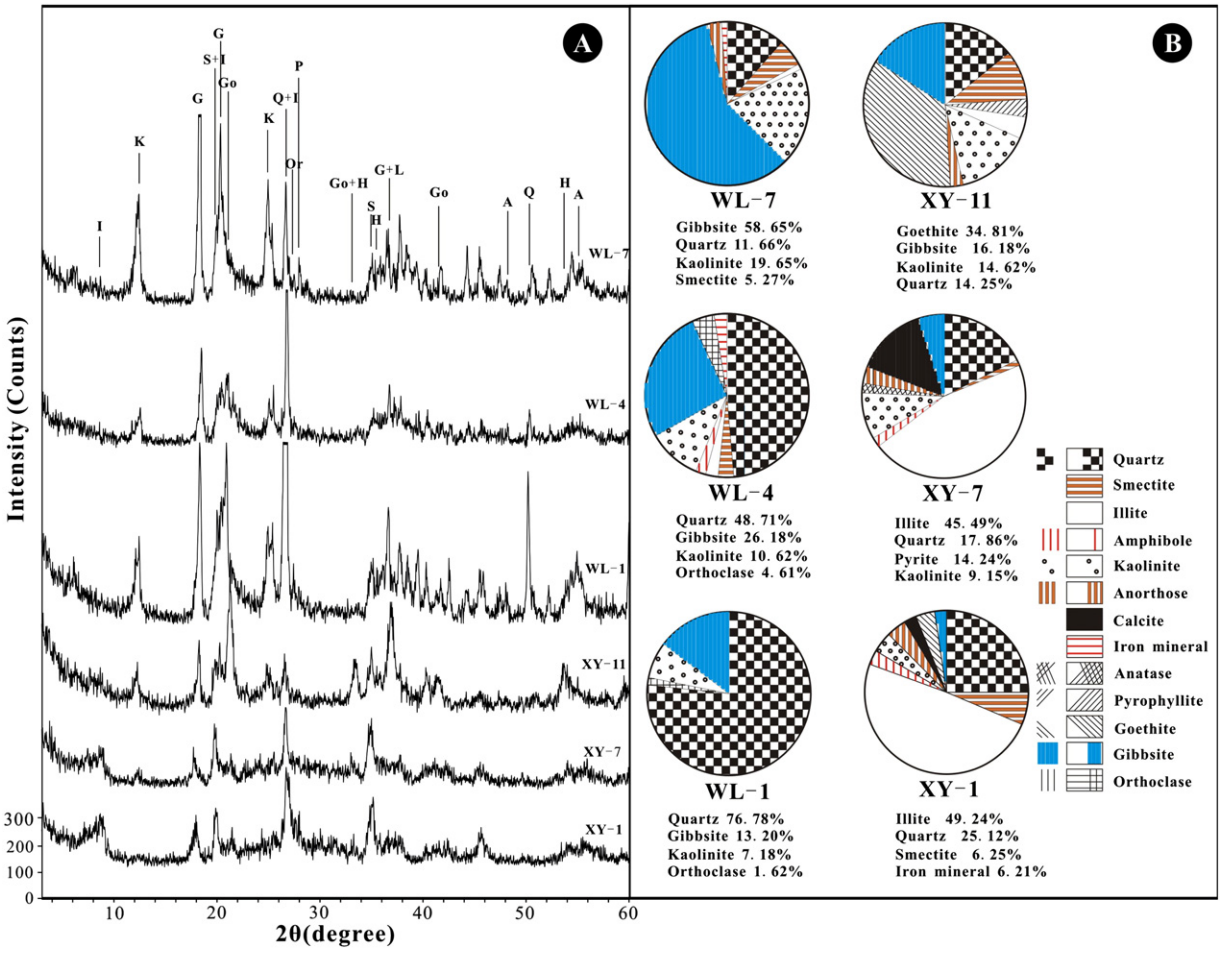

Fig. 3. (A)XRD patterns and (B) semi-quantitative calculation of mineral composition for selected ferruginous nodule and clay samples from profiles XY and WL (A—anatase, G—gibbsite, Go—goethite, H—hematite, I—illite, K—kaolinite, L—limonite, Or—orthoclase, P—pyrophyllite, Q—quartz, S—smectite).

compared with the ferruginous nodular horizon. It can be noted that there is a depletion of many siderophile elements at a depth of 280 cm. Many major and trace elements in profile WL show no significant variation throughout the profile, except in the layer at 85 cm depth (corresponding to sample WL-7) where most elements are slightly depleted. However, Al, U, Ni and Cr are highly concentrated in this layer possibly because of the relative high CIA value and weathering maturity.

Significant correlations of many elements are observed, and are shown in Fig. 8: (1) Al_2O_3 and Fe_2O_3 in lateritic profiles show significant negative correlations ($R^2 = 0.71$ in profile XY and $R^2 = 0.96$ in profile LSX); (2) SiO_2 and Fe_2O_3 display prominent negative correlation in profiles XY and LSX ($R^2 = 0.97$ and 0.99, respectively); (3) the positive correlation of Ce and Th with P_2O_5 is only observed in profile XY ($R^2 = 0.71$ for Ce and $R^2 = 0.90$ for Th); (4) SiO_2 plotted *versus* K_2O shows a significant positive correlation ($R^2 = 0.96$ in profile XY and $R^2 = 0.97$ in profile LSX); (5) Al_2O_3 and K_2O present positive correlations in the ferruginous nodular horizon of profile XY ($R^2 = 0.70$) and in the whole of profile LSX ($R^2 = 0.82$).

The chondrite normalized REE spider-diagrams of study profiles are plotted in Fig. 9, and the major characteristics of REE distribution patterns can be described as follows: (1) all samples have a negative LREE slope and flat HREE distribution, implying relative depletion of HREE compared to LREE and little HREE fractionation; (2) the pronounced positive Ce anomaly is observed in the ferruginous nodular horizon with no significant Ce anomaly in soil layers. This is indicative of sedimentation influence of Fe/Mn oxides on the enrichment of Ce; (3) the similar REE distribution patterns and δEu value (Table 1) of the three profiles suggests identical material genesis and an analogous weathering environment; (4) sample XY-7 has high LREE concentration and low HREE content comparing to the other mottled clay samples in profile XY.

5. Discussion

5.1. Genesis and formation of iron, aluminum and REE minerals

Hematite and goethite are the major iron oxide and hydroxide minerals in lateritic profiles of the study area. These are formed most likely from the oxidation of Fe released from biotite, hornblende and other ferric minerals (Nesbitt and Markovics, 1997). Although it has been well documented that kaolinite and gibbsite are common weathering products of biotite, plagioclase or other aluminosilicate minerals (Banfield and Eggleton, 1990; Dong et al., 1998; Gonzalez-Acebron et al., 2010; Jeong, 2000; Jolicoeur et al., 2000; Kretzschmar et al., 1997; MacLean et al., 1997; Rebertus et al., 1986), it is still not established that gibbsite forms directly from mica or as a weathering product of kaolinite and/or halloysite (Grant, 1962; Jolicoeur et al., 2000; Keller, 1979; Tardy, 1997). Under special conditions, kaolinite can transform into gibbsite (Jolicoeur et al., 2000; Tardy, 1997; Zheng and Ge, 1983; Zhou and Chen, 1994).

Al_2O_3 and Fe_2O_3 show significant negative correlations in the weathering covers (except for profile WL) (Fig. 8A), which is in agreement with previous findings by Liu et al. (2012) and Ji et al. (2004a). The previous interpretation for the negative correlation is that Al in the clay mineral matrix substitutes for Fe in goethite or hematite

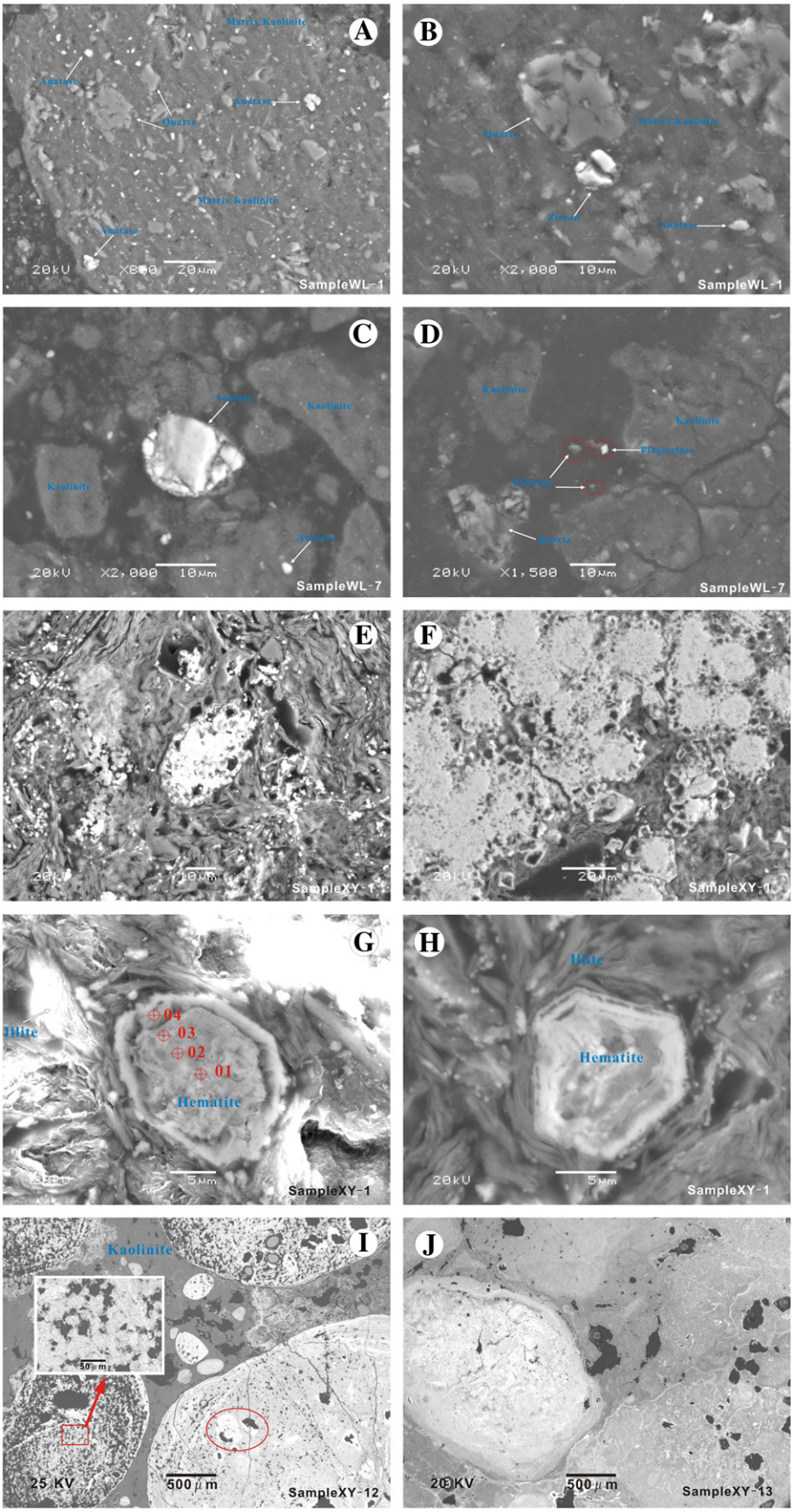
A
Matrix Kaolinite
Anatase
Anatase
Quartz
Matrix Kaolinite
Anatase
20kV X800 20μm
SampleWL-1
B
Quartz
Matrix Kaolinite
Zircon
Anatase
20kV X2,000 10μm
SampleWL-1
C
Anatase
Kaolinite
Kaolinite
Anatase
20kV X2,000 10μm
SampleWL-7
D
Kaolinite
Kaolinite
Plagioclase
Gibbsite
Quartz
20kV X1,500 10μm
SampleWL-7
E
20kV 10μm
SampleXY-1
F
20kV 20μm
SampleXY-1
G
Illite
04
03
02
01
Hematite
20kV 5μm
SampleXY-1
H
Illite
Hematite
20kV 5μm
SampleXY-1
I
Kaolinite
50μm
25 KV 500 μm
SampleXY-12
J
20KV 500 μm
SampleXY-13

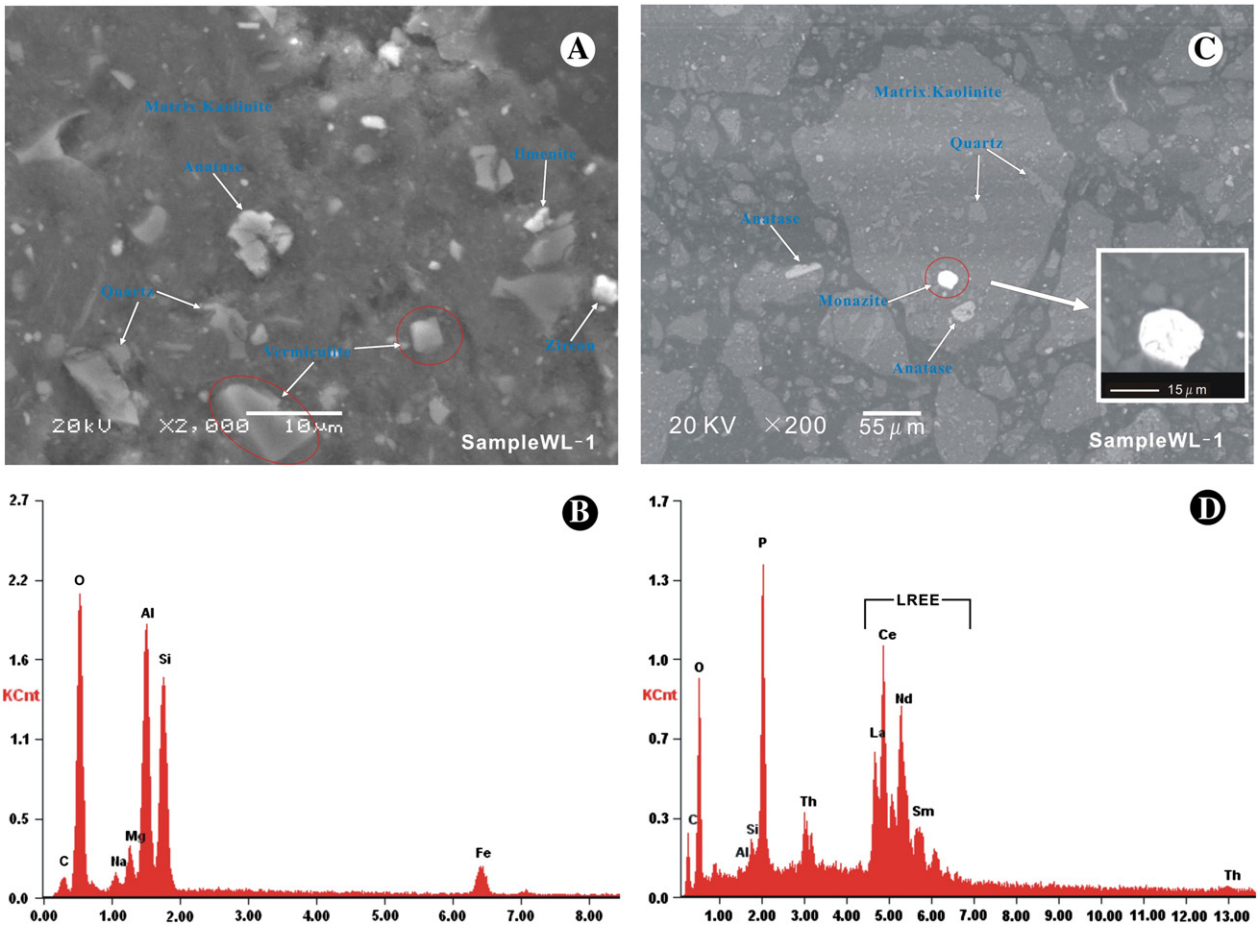

Fig. 5. SEM and EPMA observations of (A and B) Vermiculite grains replacing a former biotite. (C and D) Monazite particle in a kaolinite matrix.

(Amarasiriwardena et al., 1986; Laskou et al., 2006; Liu et al., 2012; Murad and Schwertmann, 1983; Murad and Schwertmann, 1986; Schwertmann et al., 1977; Wells et al., 2001). The SEM-EDS results are consistent with this phenomenon. For example, the ring around the hematite crystal (Fig. 4G) has a higher concentration of Al than the core, and contains some K (Fig. 10). The Fe_2O_3/Al_2O_3 ratio in illite around the hematite crystal is notably higher than that in the matrix. In this study, the exogenetic iron inputted into the ferruginous nodular horizon and upper part of mottled clay layer (Fig. 11) could be another interpretation for the negative correlation between Al_2O_3 and Fe_2O_3, because the more exogenetic Fe inputted into the system, the less relative amount of Al remained. Furthermore, this finding could be a better explanation for the dislocation of linear correlations in different layers of profile XY (in total samples, $R^2 = 0.71$; in samples of ferruginous nodular horizon, $R^2 = 0.92$; in samples of mottled layer, $R^2 = 0.96$) (Fig. 8A). It is because that there may be a difference in the amounts of exogenetic iron inputted into the two layers.

The prominent negative correlation between SiO_2 and Fe_2O_3 and the dislocation of linear correlations in different layers of profile XY likely to be associated with input of exogenetic iron (Fig. 8B).

There is a positive correlation between K_2O and SiO_2 in profiles XY and LSX (Fig. 8C), which suggests that illite might be the major K-bearing mineral in the two profiles. However, K_2O and Al_2O_3 do not correlate in the mottled clay layer (Fig. 8D), because Al changes slightly along with the variation in K_2O. This illustrates that Al was not removed during the decomposition process of illite, but was rather reserved in this system in relatively stable minerals, such as kaolinite and gibbsite (Banfield and Eggleton, 1990; Matsuoka, 1995; Nesbitt and Young, 1984; Nesbitt and Young, 1989; Ugolini, 1986).

Many reports (Abed and Sadaqah, 2013; Basu et al., 2009; Braun et al., 1998; Overstreet, 1967; Parrish, 1990; Rasmussen et al., 2001; Rice, 1973; Watson and Harrison, 1984; Wilford, 2012; Wilford et al., 2009; Wronkiewicz and Condie, 1987) suggest that Ce and Th, in regolith and sediments, are generally (1) adsorbed on clay or Fe oxides, (2) accumulated as newly formed secondary tetravalent oxides phases such as cerianite (CeO_2) and thorianite (ThO_2), (3) inherited from primary resistant minerals such as zircon and monazite, or (4) occur in secondary P-bearing phases such as apatite. In this study both Ce and Th present significant correlation with P_2O_5 in profile XY (Fig. 8E and F), suggesting that they occur primarily in phases such as monazite and

Fig. 4. SEM micrographs showing the micromorphologies of various minerals in lateritic covers in profile XY and WL. (A) Grains (including quartz, anatase and zircon) and matrix (kaolinite) in the saprolite. (B) Quartz and zircon crystals with distinct fractures and cleavages. (C) Close-up of the bigger anatase grain with fractured particle edge. (D) Plagioclase fine-grained crystal (Ø < 5 μm). The gibbsite grains present irregular form. (E) Fine iron oxide and hydroxide grains interspersed in the matrix (main is illite). (F) Abundant fine ferruginous grains concentrated together and formed big aggregates which look like sponge. (G) Secondary electronic micrograph showing the surface morphology of illite and hematite crystal. EDS point plotted corresponds to energy dispersive patterns in Fig. 11. (H) Backscattered SEM micrograph of regularly hexagonal hematite crystal with conspicuous ring belts. (I) Ferruginous nodules with many pores and fractures. The close-up indicates pores and fractures filled by ferruginous materials probably from the soil solution. (J) The porosity of ferruginous nodules decreased in surface and the boundary of the nodules and cement became blurry.

Table 1
Major elements and relevant parameters in lateritic weathering covers.

Sample	XY-1	XY-2	XY-3	XY-4	XY-5	XY-6	XY-7	XY-8	XY-9	XY-10	XY-11	XY-12	XY-13	LSX-1	LSX-2
(%)															
SiO_2	46.37	46.37	45.31	45.03	42.36	43.72	44.09	39.53	33.94	26.47	22.69	17.59	13.60	17.45	15.53
Al_2O_3	24.86	25.58	24.6	24.99	22.05	23.47	24.47	24.15	26.21	23.62	21.86	21.78	15.41	26.05	24.62
Fe_2O_3	10.02	9.44	10.97	11.00	17.50	14.36	12.49	17.39	19.49	28.44	35.13	39.96	50.36	34.23	39.43
MgO	1.92	1.88	1.91	1.81	1.76	1.81	1.75	1.57	1.07	0.86	0.74	0.57	0.56	0.42	0.37
CaO	0.058	0.059	0.085	0.071	0.062	0.066	0.078	0.051	0.11	0.11	0.12	0.10	0.081	0.12	0.11
Na_2O	0.16	0.15	0.16	0.15	0.13	0.15	0.15	0.12	0.12	0.096	0.084	0.076	0.066	0.057	0.051
K_2O	6.53	6.25	6.27	5.78	5.11	5.58	5.66	4.69	2.81	1.55	1.11	0.71	0.55	0.57	0.53
MnO	0.016	0.016	0.019	0.017	0.029	0.021	0.015	0.027	0.19	0.65	0.24	0.34	0.24	1.02	0.21
P_2O_5	0.048	0.03	0.034	0.035	0.041	0.043	0.061	0.044	0.066	0.092	0.11	0.12	0.12	0.077	0.084
TiO_2	0.91	0.98	0.99	1.02	1.01	1.07	1.14	1.20	1.52	1.67	1.71	1.62	1.64	2.08	1.65
L.O.I.	8.90	9.05	9.46	9.94	9.80	9.62	9.84	11.19	14.26	15.95	15.98	16.70	16.79	17.46	16.89
Total	99.79	99.81	99.81	99.84	99.85	99.91	99.74	99.96	99.79	99.51	99.77	99.57	99.42	99.53	99.48
A/S	0.54	0.55	0.54	0.55	0.52	0.54	0.56	0.61	0.77	0.89	0.96	1.24	1.13	1.49	1.59
CIA	77.23	78.49	77.73	79.35	79.33	78.87	79.34	82.08	89.00	92.79	94.23	96.06	95.63	97.34	97.40

A/S refers to the concentration ratio of Al_2O_3 and SiO_2.
Chemical index of alteration (CIA) = $Al_2O_3/(Al_2O_3 + CaO^* + Na_2O + K_2O) \times 100$, using molecular proportions, where CaO^* is amount of CaO incorporated in silicate fraction of the rock (Nesbitt and Young, 1982).

apatite. In the other two lateritic regolith profiles, monazite was not the main carrier for Ce and Th.

5.2. Mobilization and redistribution of elements

5.2.1. Major elements

Si, Al, Na and K in profiles XY and LSX are all characterized by mass loss in the ferruginous nodular horizon, and they show slight mass loss in the mottled clay layer and top soil layer (Fig. 11). This may be the result of kaolinization of feldspars and subsequent breakdown of kaolinite (Calagari and Abedini, 2007). Mineralogical investigation by XRD indicates that large quantities of Si are fixed by clay minerals, muscovite, amphibole and quartz. Al is present primarily in the form of illite in the mottled clay layers, whereas gibbsite is the main carrier of Al in the ferruginous nodular horizon. Significant mass loss of K occurred in the ferruginous nodular horizon, because when illite altered to kaolinite and

Table 2
Trace elements, REE and relevant parameters in lateritic weathering covers.

Sample	XY-1	XY-2	XY-3	XY-4	XY-5	XY-6	XY-7	XY-8	XY-9	XY-10	XY-11	XY-12	XY-13	LSX-1	LSX-2
(ppm)															
Li	26.7	28.4	24.7	28.7	23.2	22.8	28.5	33.1	46.4	56.7	30.6	33.8	29.1	39.2	16.7
V	195	182	201	210	199	251	225	274	455	667	733	900	952	819	765
Cr	154	131	148	162	156	159	167	189	287	385	424	512	580	434	388
Co	8.12	6.46	7.55	8.89	8.46	11.6	7.91	9.85	79.8	213	84.9	111	92.8	121	34.5
Ni	46.6	33.2	40.9	32.6	43.4	38.2	29.4	35	94.4	165	109	163	137	120	60.4
Cu	65.4	74.4	67.8	83.1	74.3	70.2	82.9	125	155	172	150	191	175	178	127
Zn	128	108	151	102	157	108	81	107	273	553	523	650	694	284	188
Rb	213	136	222	214	196	228	215	155	98.9	69.9	55.3	38.5	33.9	34.2	29.9
Sr	21.3	14.7	23.3	26.1	24.3	33.1	35.7	28.8	33.9	33.1	31	36.7	33.6	34.7	28.2
Nb	16.7	16.3	17.1	19	16.6	18.1	21.4	21.6	27.9	30.8	29.8	37.2	34.9	40.9	34.6
Cs	30.3	25.2	30.7	31.9	27.1	27.9	30.8	25.8	19.7	13.8	11.7	9.07	8.4	7.06	5.66
Ba	541	393	514	514	442	571	534	433	270	261	146	120	92.1	189	80.4
Ta	1.17	1.2	1.29	1.41	1.22	1.34	1.58	1.61	2.11	2.3	2.22	2.69	2.71	3.03	2.51
Th	19.5	12.8	21	22.4	21.2	22.8	24.5	25.4	31.4	38.8	38.8	39.6	44.9	54.3	46.8
Zr	212	205	216	243	220	251	268	257	348	392	403	456	435	469	403
Hf	5.72	5.45	6.11	6.76	5.73	6.36	7.73	7.02	9.38	10.4	10.9	11.4	11.2	13.4	11
La	42	31.5	53.1	65.4	50.8	67.2	98.6	46.7	63.4	74.9	69.1	73.4	72.8	59.3	50.6
Ce	94.4	72.7	111	122	105	129	173	87.4	202	389	239	466	241	472	182
Pr	10.2	7.25	12.1	13	10.4	13.5	26.5	10	12.8	16.9	15.8	16.2	17.5	11.9	9.93
Nd	38.8	28.2	46.1	47.2	39.2	52.1	97.9	37.7	45.6	60.5	58.9	64.9	69.3	42.8	35.1
Sm	6.35	4.94	9.11	7.53	7.2	8.22	15.7	6.37	8.25	12	11.9	13.3	15.2	8.16	6.79
Eu	1.34	0.97	1.84	1.47	1.43	1.51	2.65	1.18	1.7	2.45	2.6	2.83	2.92	1.61	1.35
Gd	6.11	4.47	9.03	6.77	6.91	7.25	10.8	4.91	8.25	12.9	12.5	14.9	15.8	9.21	6.4
Tb	1.01	0.767	1.63	1.12	1.15	1.08	1.59	0.859	1.39	2.21	2.33	2.66	2.94	1.47	1.14
Dy	6.39	4.52	9.52	6.79	6.64	6.52	7.93	4.76	8.73	13.1	14.7	16.2	18.5	8.04	6.46
Ho	1.27	0.878	1.78	1.27	1.32	1.09	1.38	1	1.79	2.66	2.97	3.39	3.83	1.58	1.29
Er	3.75	2.79	5.41	3.98	3.87	3.82	4.27	3.21	5.47	8.08	9.19	10	11	4.84	3.94
Tm	0.56	0.465	0.886	0.688	0.646	0.545	0.672	0.579	0.86	1.21	1.34	1.57	1.75	0.831	0.687
Yb	4.01	2.97	5.46	3.97	4.02	3.87	4.18	3.43	5.5	7.56	7.86	9.27	11	5.28	4.29
Lu	0.599	0.436	0.822	0.673	0.63	0.579	0.638	0.56	0.83	1.18	1.3	1.46	1.61	0.857	0.687
∑REE	216.79	162.86	267.79	281.86	239.22	296.28	445.81	208.66	366.57	604.65	449.49	696.08	485.15	627.88	310.66
LREE	193.09	145.56	233.25	256.60	214.03	271.53	414.35	189.35	333.75	555.75	397.30	636.63	418.72	595.77	285.77
HREE	23.70	17.30	34.54	25.26	25.19	24.75	31.46	19.31	32.82	48.90	52.19	59.45	66.43	32.11	24.89
L/H	8.15	8.42	6.75	10.16	8.50	10.97	13.17	9.81	10.17	11.37	7.61	10.71	6.30	18.56	11.48
δCe	1.10	1.16	1.05	1.01	1.10	1.03	0.81	0.97	1.71	2.63	1.74	3.25	1.63	4.28	1.95
δEu	0.66	0.63	0.62	0.63	0.62	0.60	0.62	0.65	0.63	0.60	0.65	0.61	0.58	0.57	0.63

∑REE = the sum of La–Lu, $\delta Ce = Ce_N/(La_N \times Pr_N)^{0.5}$, $\delta Eu = Eu_N/(Sm_N \times Gd_N)^{0.5}$, where N refers to a chondrite-normalized value (Taylor and McLennan, 1985).

LSX-3	LSX-4	LSX-5	LSX-6	LSX-7	LSX8	WL-1	WL-2	WL-3	WL-4	WL-5	WL-6	WL-7	WL-8	WL-9
14.62	12.38	14.29	15.02	29.67	29.07	44.27	35.86	34.73	33.7	37.81	40.4	31.31	38.09	37.64
22.59	22.17	22.49	21.67	30.86	29.53	28.74	32.23	31.81	32.86	30.68	33.48	43.22	36.1	34.46
42.21	45.63	42.67	42.29	17.7	19.69	6.32	9.24	10.63	10.09	8.46	3.47	1.46	3.64	3.73
0.40	0.37	0.41	0.54	0.57	0.63	0.41	0.42	0.44	0.42	0.43	0.36	0.25	0.36	0.36
0.12	0.10	0.14	0.22	0.30	0.30	0.12	0.12	0.13	0.09	0.087	0.089	0.2	0.26	0.38
0.049	0.047	0.053	0.071	0.091	0.084	0.100	0.095	0.089	0.092	0.087	0.097	0.088	0.120	0.150
0.53	0.51	0.53	0.57	1.25	1.32	0.62	0.6	0.63	0.55	0.46	0.56	0.43	0.55	0.55
0.950	0.880	0.550	0.190	0.071	0.083	0.043	0.021	0.021	0.025	0.056	0.012	0.007	0.020	0.018
0.085	0.096	0.097	0.13	0.073	0.077	0.14	0.19	0.20	0.18	0.15	0.15	0.17	0.15	0.20
1.54	1.49	1.58	1.68	2.13	2.09	4.81	3.51	3.26	2.98	3.68	3.84	2.07	3.87	3.62
16.41	16.28	16.77	17.29	17.00	16.99	14.04	17.13	17.72	18.71	17.65	17.26	20.43	16.51	18.45
99.50	99.95	99.58	99.67	99.72	99.86	99.61	99.42	99.66	99.70	99.55	99.72	99.63	99.67	99.56
1.55	1.79	1.57	1.44	1.04	1.02	0.65	0.90	0.92	0.98	0.81	0.83	1.38	0.95	0.92
97.19	97.24	97.15	96.72	95.36	94.96	97.17	97.56	97.46	97.78	97.95	97.76	98.61	97.85	97.61

gibbsite, large amounts of K entered into soil solution during weathering. Similarly, Na has undergone mass transfer in the ferruginous nodular horizon as a result of plagioclase breakdown. However, the concentration of Na is one order of magnitude lower than that of K in the two profiles (Fig. 7). This may have resulted from the fixing of K in illite or other K-bearing minerals (such as muscovite). Another reason for this is that K has larger cation radius than Na being preferentially adsorbed and retained on clay minerals (Coleman et al., 1959; Sumner et al., 1996; White et al., 1996).

The elements Mg, Mn and Fe were probably released from decomposition of ferromagnesian minerals. The high mass loss of Mg in the upper part of the two profiles may be attributable to the lower content of chlorite compared to the lower section. Conversely, there is a mass increase of Fe in the ferruginous nodular horizon and upper part of mottled clay layers of profile XY, which illustrates that there was exogenetic input of

LSX-3	LSX-4	LSX-5	LSX-6	LSX-7	LSX8	WL-1	WL-2	WL-3	WL-4	WL-5	WL-6	WL-7	WL-8	WL-9
39.7	31.9	29.5	20.9	32.4	35.9	43.4	67.3	61.5	61.7	46.7	37.4	41.5	44.2	44.8
935	922	904	834	374	463	403	342	335	343	275	242	223	267	291
386	378	438	655	211	307	240	196	191	196	171	184	250	199	227
147	221	77.7	37.5	12.9	20.7	10.8	13.5	12.8	12.5	11.6	7.85	7.28	10.7	14.6
171	137	101	67.2	53	65.5	56.1	62.8	72.1	75.8	57.8	51.1	79.7	58.4	59.9
190	161	144	127	90.2	111	54.2	63.6	68.8	62.6	50.6	44.1	49.2	45.8	50.5
241	212	230	255	142	186	201	223	201	205	182	127	185	150	160
27.9	25.8	30.8	25.6	56.1	68.2	36.3	34.6	50.2	44.3	29.3	32.6	22.3	32.7	25.7
22.7	15.7	21.7	20.3	31.3	34.6	117	82.1	82.5	72.9	68.8	100	102	116	67.5
37.2	33.4	35.2	37.4	37.5	42.9	80.5	73.2	62.7	57.6	58.5	67.4	46.3	71.2	70
5.87	4.94	6.49	7.88	14	15.7	10.3	11.8	12.6	12.9	10.4	10.2	6.45	8.89	4.31
176	99.1	119	63.2	127	162	192	169	182	175	125	170	189	206	174
2.75	2.5	2.64	2.8	2.73	3.17	5	5.35	5.08	4.55	4.76	5.6	3.75	6.02	5.95
38.6	37.9	37.9	26.2	22.7	29.7	44.6	47.3	46.9	45	39.1	42.8	49.2	47.7	48.1
456	390	437	452	399	459	882	722	611	594	605	690	555	874	834
12.8	10.7	12.3	12.6	11.1	12.7	27.1	22.9	17.7	17.9	17.9	20.9	16.7	26.6	26.4
53.9	42.7	49	38.1	38.7	47.5	133	108	109	113	87.5	123	148	149	115
974	566	621	94.5	59.7	81.3	213	176	191	199	141	186	224	223	190
10.5	8.67	10.1	8.24	7.14	9.06	25.4	20.5	21.7	22.2	16.9	24.3	31.1	29.4	22.5
40.7	29.9	36.5	30.7	24.3	31.7	88.3	79.8	77.1	78.8	59.1	87.9	116	103	78.8
8.92	5.57	6.78	6.09	3.96	5.3	13.2	12.7	12.4	12.7	9.6	14.2	19.8	16.7	11.9
1.72	1	1.38	1.21	0.769	0.987	2.54	2.51	2.22	2.39	1.77	2.56	3.64	2.98	2.09
11.2	6.66	7.85	5.28	3.46	4.65	11.8	12.4	10.4	10.5	8.3	11.6	15.8	12.8	10.2
1.38	0.908	1.18	0.979	0.655	0.892	2.07	1.85	1.84	1.84	1.47	2.03	2.45	2.22	1.61
7.25	4.81	6.16	5.16	3.8	5.08	11.5	12.1	10	10.5	8.58	10.9	12	12.5	8.84
1.29	0.96	1.16	1.06	0.803	1.04	2.25	2.42	1.96	2.06	1.74	2.03	1.91	2.32	1.55
3.82	2.94	3.48	3.13	2.5	3.16	6.88	6.88	6.06	6.25	5.13	6.12	5.47	7	4.94
0.761	0.477	0.592	0.511	0.416	0.55	1.19	1.28	1.02	1.03	0.896	1.05	0.839	1.19	0.826
4.82	3.12	3.75	3.28	2.73	3.42	8.04	7.88	6.95	6.7	6.12	6.65	5.39	7.79	5.55
0.599	0.522	0.6	0.554	0.456	0.562	1.3	1.09	1.07	1.08	0.991	1.02	0.821	1.21	0.885
1120.86	674.24	749.53	198.79	149.39	195.20	520.47	445.41	452.72	468.05	349.10	479.36	587.22	571.11	454.69
1089.74	653.84	724.76	178.84	134.57	175.85	475.44	399.51	413.42	428.09	315.87	437.96	542.54	524.08	420.29
31.12	20.40	24.77	19.95	14.82	19.35	45.03	45.90	39.30	39.96	33.23	41.40	44.68	47.03	34.40
35.02	32.06	29.26	8.96	9.08	9.09	10.56	8.70	10.52	10.71	9.51	10.58	12.14	11.14	12.22
9.85	7.08	6.72	1.28	0.86	0.94	0.88	0.90	0.95	0.96	0.88	0.82	0.79	0.81	0.90
0.53	0.50	0.58	0.65	0.64	0.61	0.62	0.61	0.60	0.63	0.61	0.61	0.63	0.62	0.58

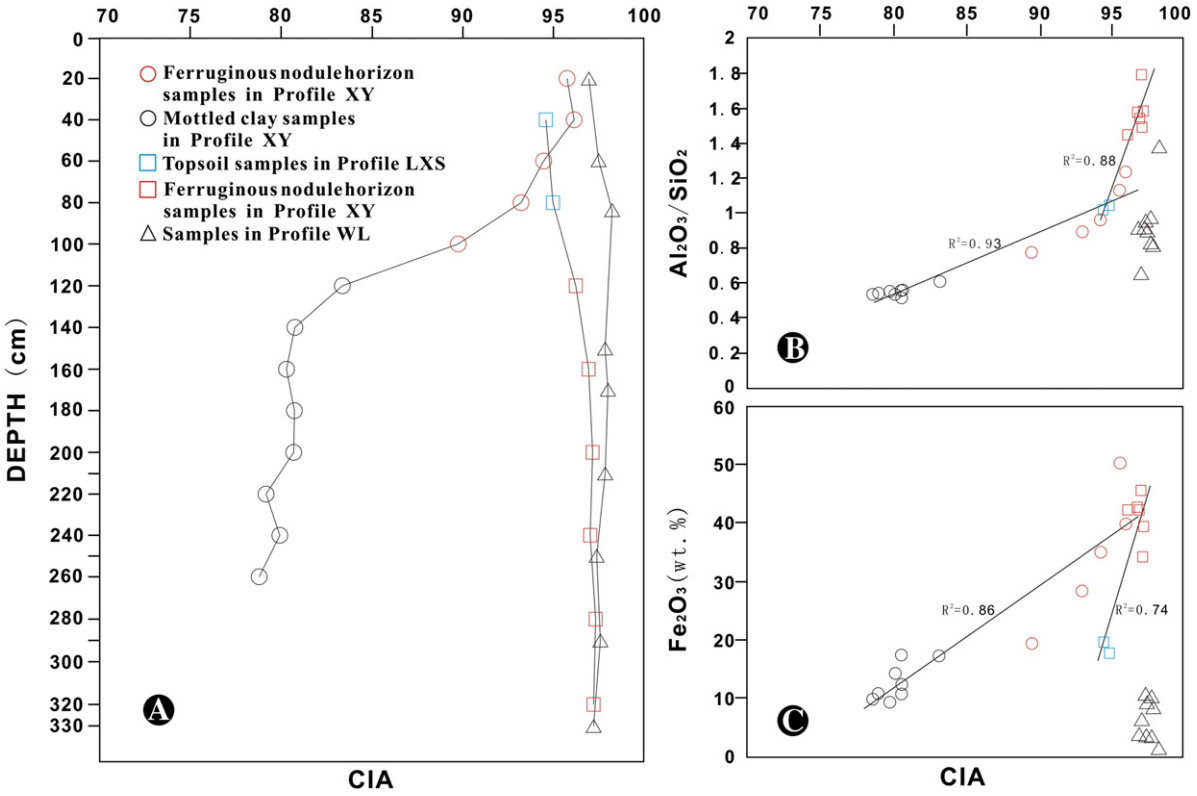

Fig. 6. (A) Relationships of depth and CIA values and (B–E) distributions of K_2O, Na_2O, Al_2O_3/SiO_2 and Fe_2O_3 *vs.* CIA values. High CIA values in profile LSX and WL and low in profile XY are seen in diagram A, and significant variation of CIA is observed in the ferruginous nodular horizon of profile XY. Prominent negative (K_2O and Na_2O *vs.* CIA) and positive correlations (Al_2O_3/SiO_2 and Fe_2O_3 *vs.* CIA) are in profile XY and LSX.

Fe into these layers, compared to the bottom layer of the profile. The exogenetic Fe may have originated from leaching and subsequent migration of Fe from the inchoate lateritic horizon that overlies the ferruginous nodular horizon. The mass depletion of Fe in the top soil layer of profile LSX is consistent with this finding. Generally, the stability of Mn in solution depends on the valence state. Bivalent manganese (Mn^{2+}) is easily transferred into soil solution, whereas tetravalent manganese (Mn^{4+}) usually precipitates stably (Liu et al., 1984). The mass increase of Mn (not shown) in the ferruginous nodular horizon of the two profiles is probably the result of Fe oxide precipitation and supergene enrichment. There is no significant mass transfer of Ti throughout the whole profile. This illustrates that Ti is stable and homogeneously distributed during weathering, and the two profiles represent an *in situ* weathering crust without exogenetic material source input.

5.2.2. Trace element

Mass transfer coefficients of selected trace elements in the two profiles are plotted in Fig. 11. Many high field strength elements (HFSE), such as Nb, Ta, Hf, and Th show no significant mass change throughout the two profiles. However, Th displays mass depletion in the lower part of profile XY (sample XY-2) and top soil layer of profile LSX (sample LXS-6, 7, 8). This finding suggests that the HFSE were immobile during weathering, and this profile represents an *in situ* weathering residuum. Braun et al. (1998) found that Th is immobile in the supergene environment, whereas Th removal and mobility is enhanced by organic matter. There is a mass increase in V, Cr, Ni, Cu and Zn in the ferruginous nodular horizon, and they show no significant mass change or mass loss (*e.g.* Ni and Zn) in the mottled clay layer and topsoil layer. This illustrates that the enrichment of these elements resulted from the precipitation of ferromanganese and Fe oxides, which have a strong adsorption capacity (Liu et al., 1984).

Mass loss of Rb, Cs, Ba, Li and Sr has occurred in the ferruginous nodular horizon and topsoil layer, and a slight mass loss in the mottled clay layer. The depletion is likely due to the higher mobility of alkali and alkali earth metals during weathering. However, ferromanganese precipitation does not fix these elements. Specifically, clay minerals strongly adsorb Sr, mainly in the upper part of the clay layers.

Generally, U is mobile in the supergene weathering environment, *i.e.* under strong oxidation, because U^{6+} can easily form a soluble complex (uranyl) (Braun et al., 1990; Ji et al., 2004a; Liu et al., 1984). However, adsorption of U on minerals such as hematite and goethite and occlusion of U by Fe-oxide coatings can retard U transport (Ching-kuo Daniel and Langmuir, 1985; Duff and Amrhein, 1996; Duff et al., 2002; Read et al., 1993). The mass increase of U in the ferruginous nodular horizon possibly resulted from adsorption onto Fe oxides, whereas the slight mass increase in the middle part of the mottled clay layer may be related to the reducing environment induced by metal-reducing bacteria or humic acid(Duff et al., 1999; Duff et al., 2002).

5.2.3. Rare earth elements

The mass balance calculations show evidence of fractionation among LREE (La to Nd), middle REE (Sm to Dy) and HREE (Ho to Lu) in the ferruginous nodular horizon of profile XY, but no obvious fractionation in profile LSX (Fig. 11). This is likely related to the occurrence of profile XY at the bottom of the ferruginous nodular horizon, and profile LXS in the upper part of the ferruginous nodular horizon. This phenomenon is similar to the dolomite weathering crust described by Ji et al. (2004b). In the mottled clay layer and boundary (horizon of sample XY-8 and XY-9), most REE show mass depletion. The upper section of the clay layer (horizon of sample XY-7) is characterized by the mass increase of LREE and mass depletion of HREE as shown in the chondrite normalized REE spider-diagrams (Fig. 9). The REE pattern likely results from HREE being preferentially leached and removed compared to LREE in the supergene environment(Aubert et al., 2001; Braun et al., 1998; Caspari et al., 2006; Ji et al., 2004b; Laveuf and Cornu, 2009; Mongelli, 1993).

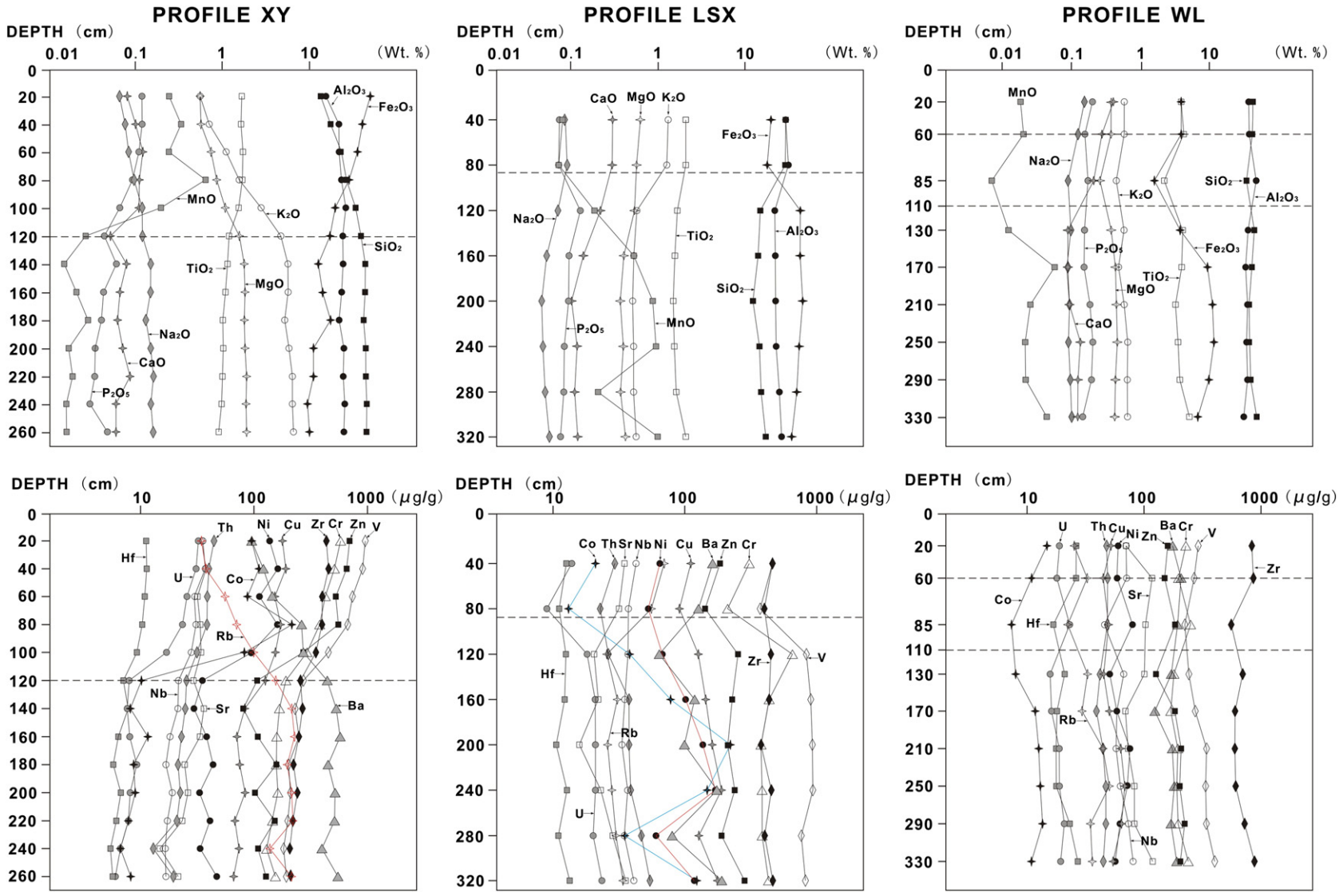

Fig. 7. Vertical distribution major elements (in wt.%) and trace elements (inμg/g) in three representative weathering profiles (XY, LSX and WL). The dotted line indicate approximate position of boundary between different layers.

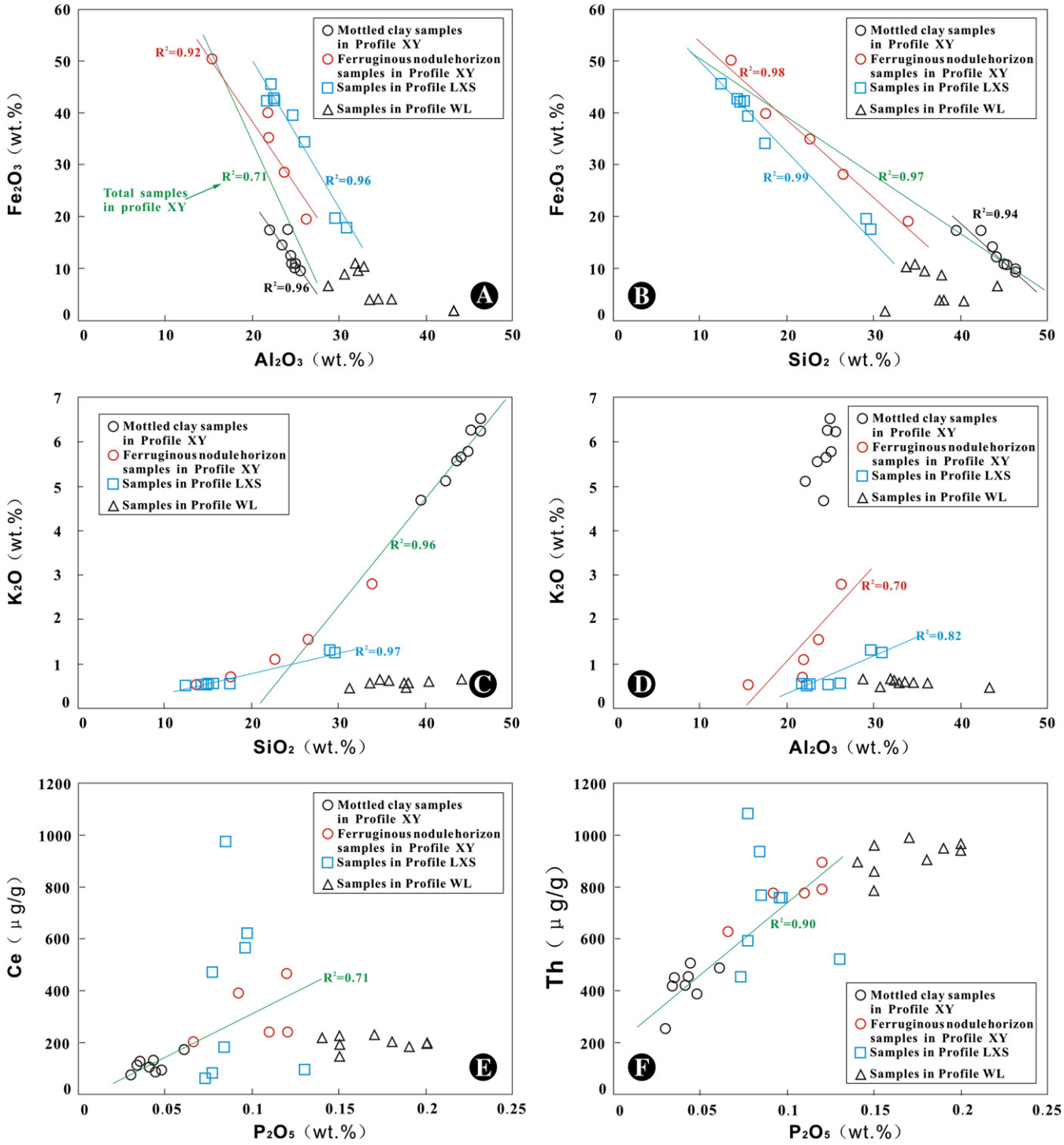

Fig. 8. Distribution of (A) Fe_2O_3 *vs.* Al_2O_3, (B) Fe_2O_3 *vs.* SiO_2, (C and D) SiO_2 and Al_2O_3 *vs.* K_2O and (E and F) Ce and Th *vs.* P_2O_5. Significant correlations are shown in the plots.

Fig. 9 also displays that REEs are concentrated in the bottom of the mottled clay layer (sample XY-3).

The content of Ce shows a prominent mass increase in the ferruginous nodular horizon, especially in layers of sample XY-10 and XY-12 (Fig. 11). Furthermore, Fig. 9 displays distinct positive Ce anomalies in the ferruginous nodular horizon, while there is no significant Ce anomaly in the mottled clay layer ($\delta Ce \approx 1$). This anomaly indicates that Fe and Mn oxides in the ferruginous nodular horizon have adsorbed and promoted sedimentation of Ce. It has been documented that Ce is preferentially trapped by Fe and Mn oxides(Laveuf and Cornu, 2009; Ma et al., 2002), and that soil, nodules, concretions and coatings that include such oxides commonly display positive Ce anomalies(Land et al., 1999; Marques et al., 2000; Palumbo et al., 2001; Rankin and Childs, 1976; Steinmann and Stille, 1997; Xing and Dudas, 1993). The fluctuation of Ce may be explained by a succession of varying periods of weathering intensity and redox environment caused by climatic change (Braun et al., 1998; Xi, 1990; Ji et al., 2004b).

A negative Eu anomaly occurs in the whole profile but there is a lack of large amplitude variation ($\delta Eu \approx 0.6$) (Fig. 9). Feldspar is considered to be the primary silicate mineral responsible for the positive Eu anomaly and thus the decomposition of feldspar leads to a negative Eu anomaly (Aubert et al., 2001; Chase et al., 1963; Compton et al., 2003; Halla

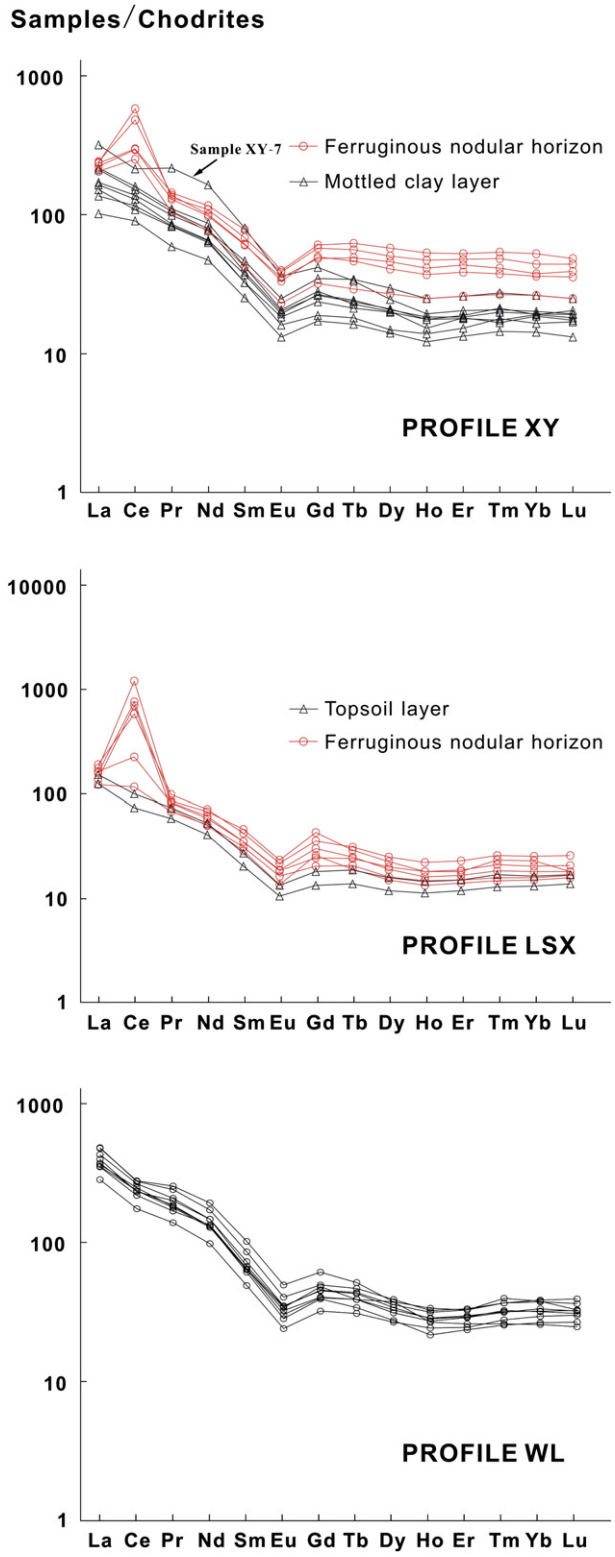

Fig. 9. Chondrite-normalized REE patterns for topsoil layer, ferruginous nodular horizon and mottled clay layer in typical weathering profiles (XY, LSX and WL).

et al., 2009; Henderson, 1984; Schaetzl et al., 2006; Towell et al., 1969). Analysis of the mineral composition indicates that the content of feldspar increases with the depth in the profile. The variation in δEu is not consistent with the concentration of plagioclase, and it is thus postulated that the redox conditions of the parent rock may have been an influencing factor on Eu.

5.3. Formation and evolution model of lateritic profile

5.3.1. Formation condition

a. Climatic factor: The study area is located 1° south of the Tropic of Cancer, and is thus influenced by the tropical monsoon climate. The high temperatures and abundant rainfall create favorable condition for deep chemical weathering and pedogenesis. Physical, chemical and biological weathering is intensive under this climate, and wet and dry seasons alternate. Generally, the hematite/goethite (He/Gt) ratio can be employed as a tool to assess short-term variation in humidity and aridity caused by climate and the groundwater table (Braun et al., 1990, 1998; Ji et al., 2004c; Tardy and Nahon, 1985). The composition and stability fields of Fe and Al oxide solid solutions depend on aqueous activity and the Fe/Al ratio (Tardy and Nahon, 1985). Goethite is commonly associated with hematite in nature. For example, a small concretion of Fe oxide was visible from SEM analysis which was investigated at a lamina-scale for the mole fraction ratio of O and Fe. Variation in the He/Gt ratio is reflected by a curve in Fig. 12. Points 5 and 6 in the SEM image have lower He/Gt ratios, consistent with a more arid environment than that of the other laminae. Furthermore, fluctuation of the mass transfer coefficient of Ce in the ferruginous nodular horizon confirms the variation in climate and environment (Braun et al., 1990, 1998; Ji et al., 2004b).
b. Geomorphological factor: Karst plains and low hills predominate in the study area. The gentle slopes (3–10°) are stable for thick lateritic weathering crust development. These geomorphic units are commonly controlled by the stratigraphy and tectonics.
c. Lithological factor: Widespread lateritic weathering crusts formed in the Quaternary generally overlie carbonate rocks of the Devonian and Carboniferous. Although carbonate rocks are the main lithology, illite is the dominant clay mineral in profile XY. Dissolution of carbonate rock increases the pH of surface and ground water, which is beneficial for the removal of silica and the formation of kaolinite and gibbsite.
d. Tectonic factor: Tectonic uplift since the Tertiary accelerated weathering and laterization, while faults and fractures improved rock permeability and drainage, increasing the rate of water–rock reaction.

5.3.2. Evolution model

Based on the formation model of ferruginous concretion proposed by Tardy and Nahon (1985) and Tardy (1997), the local natural conditions (climate, geomorphology, lithology and tectonics) and the mineralogical and geochemical evidence, we established an evolution model for lateritic weathering cover in south-central Guangxi (Fig. 13). It is anticipated that this model will be beneficial for local prospecting and environmental research. The model can be summarized as follows:

Incipient weathering of bedrock began with the decomposition and dissolution of primary minerals such as calcite, feldspar and biotite. However, relatively weathering-resistant primary minerals such as K-feldspar and muscovite were conserved in the incipient weathering products. Subsequently, clay minerals (such as kaolinite and illite) formed in abundance, and the original soil layer was preserved covering the bedrock (Fig. 13A). In terms of major element geochemistry K, Na, Ca and Mg were leached and removed by soil solution, whereas Al, Fe and Ti remained. Meanwhile, Fe^{2+} released from Fe-bearing primary minerals was oxidized to form Fe oxides and hydroxides. These Fe-bearing minerals progressively accumulated into fine grains and then formed spongy aggregates. During this period, the groundwater table was shallow and Fe occurred mainly in the form of goethite due to increased aqueous activity (Tardy and Nahon, 1985).

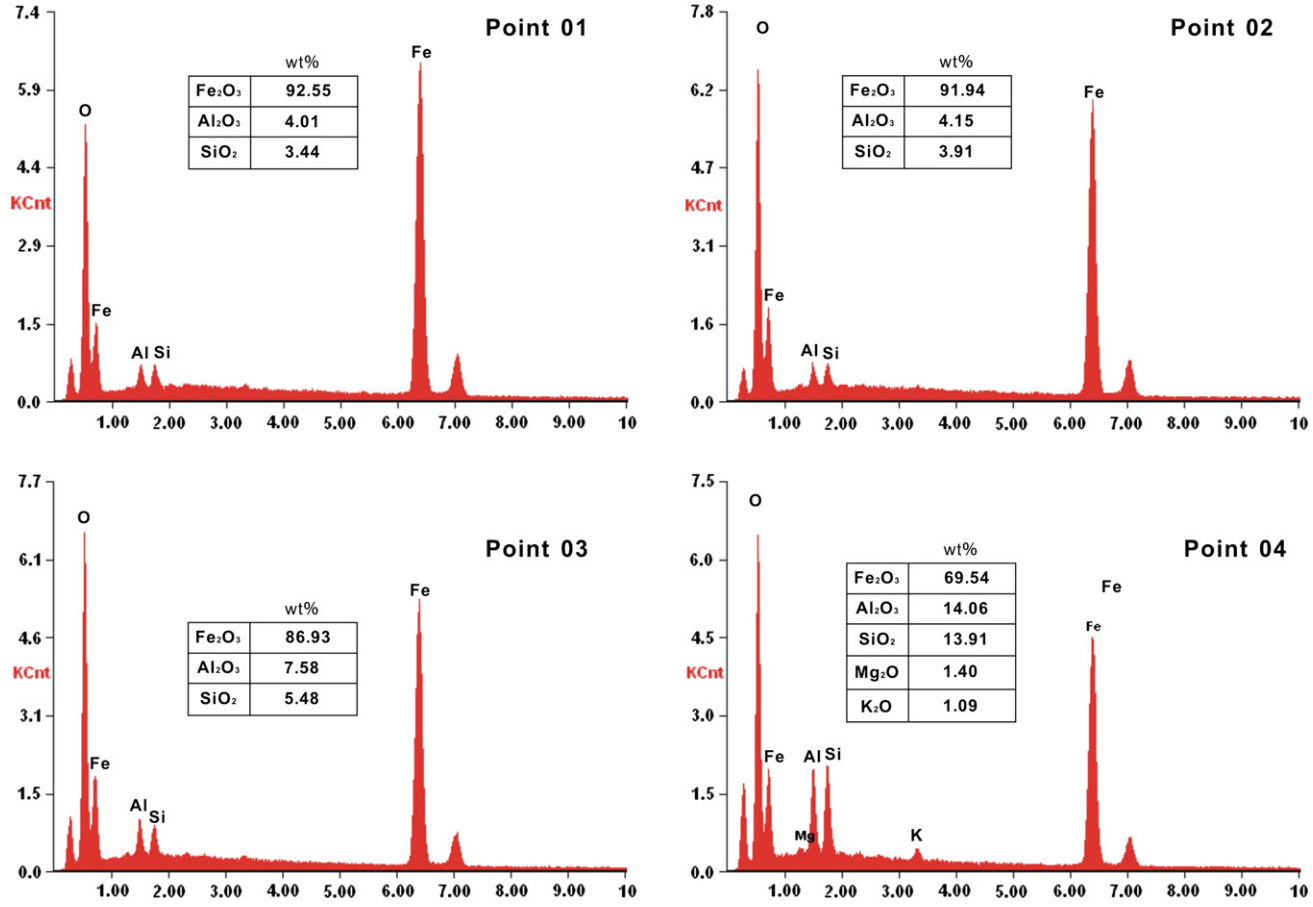

Fig. 10. Energy dispersive pattern and oxides composition (in wt. %) of the hematite crystal displayed in Fig. 4G.

Over time, the weathering front moved downward resulting in alteration of the parent rock, and the former water table zone becoming unsaturated (Fig. 13B). Meanwhile, Fe oxides aggregated, forming larger iron nodules and concretions with high porosity and other minerals, such as clays, quartz, zircon and anatase, became ingrained in the nodules. Under ideal drainage conditions, K was largely leached and thus illite progressively altered to kaolinite. In the whole process of laterization, Al^{3+} in both the clay matrix and mineral grains involved in iron nodules exchanged with Fe^{3+} in iron nodules and concretions. Moreover, Fe-rich material in the soil solution (*e.g.* Fe^{3+} and colloidal Fe hydroxide) migrated downward and horizontally, precipitating on the coating, pores and fractures of previously generated iron nodules. Because of increased aqueous activity, the sedimentary Fe-rich material was mainly goethite, characterized by a higher Fe/Al content ratio than the iron nodules. The EDS results confirm that the later sedimentary Fe coating and filler have a relatively high Fe/Al ratio. Subsequently, several iron nodules were cemented by kaolinite and Fe-rich material in the matrix and formed compound ferruginous gravels of various sizes. Finally, a thin iron nodule horizon formed overlying the saprolite (Fig. 13B).

As the degree of weathering deepened, the overall thickness of the weathered crust increased and the regional ferruginous nodular horizon became exposed by the weathering and denudation (Fig. 13C). On the microscopic scale, the cements and nodules of the ferruginous gravels developed further and became more varied. The cements changed from kaolinite to gibbsite by removal of silica, and the Fe content of the cements increased slightly. The porosity of iron nodules decreased and the nodule-cement boundary became diffuse (Fig. 4J). We postulate, therefore, that the exchange of material between iron nodules and cements led to progressive homogenization of the inside of the iron nodules.

6. Conclusions

From the above study, with focus on the geochemical and mineralogical characteristics of the study area, the following conclusions can be drawn:

(1) The tropical lateritic weathering covers of south-central Guangxi are deeply weathered products of parent rocks. The lateritic profiles contain predominantly goethite, hematite, gibbsite, illite and kaolinite, while anatase, quartz, zircon and biotite are common accessory minerals. The ferruginous nodules and concretions are characterized by high concentrations of Fe and Al and low contents of Si.

(2) During the formation process of ferruginous nodules, voids and fractures of nodules were filled with ferruginous materials derived from soil solution, and nodules maintained element exchanges with clay matrix.

(3) The mass balance calculation results show that there is exogenetic input of iron into lateritic covers, especially within the ferruginous nodular horizon, which interprets the negative correlations between Fe_2O_3 and Al_2O_3. The concentration of Ce in ferruginous nodular horizon and accumulation of Sr in mottled clay layer indicate that Fe and Mn oxides have an apparent effect on precipitating Ce, and clay minerals have higher adsorption capacity to Sr, respectively.

(4) Goethite and hematite are the primary carriers of Fe in the lateritic soils and iron nodules. Variation in the He/Gt ratio reflected by the O/Fe ratio in a small Fe oxide concretion indicates that climate changes altered aqueous activity of the soil environment. Alternatively, the change of wet and dry seasons led to fluctuation of the groundwater table.

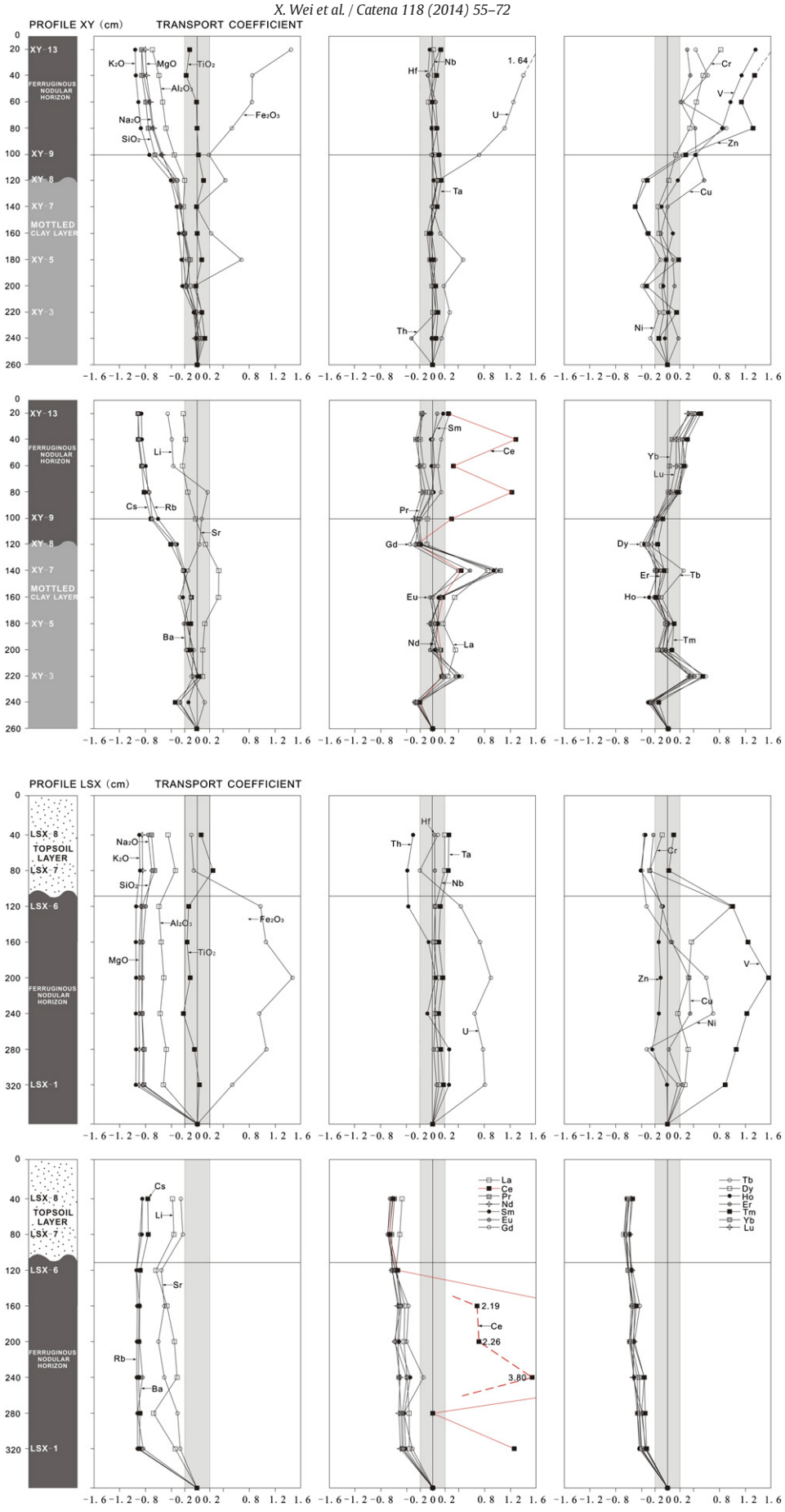

Fig. 11. Depth profiles and transport coefficient for selected major, trace and rare earth elements in profile XY and LSX. Sample XY-1 represents fresh parent rock.

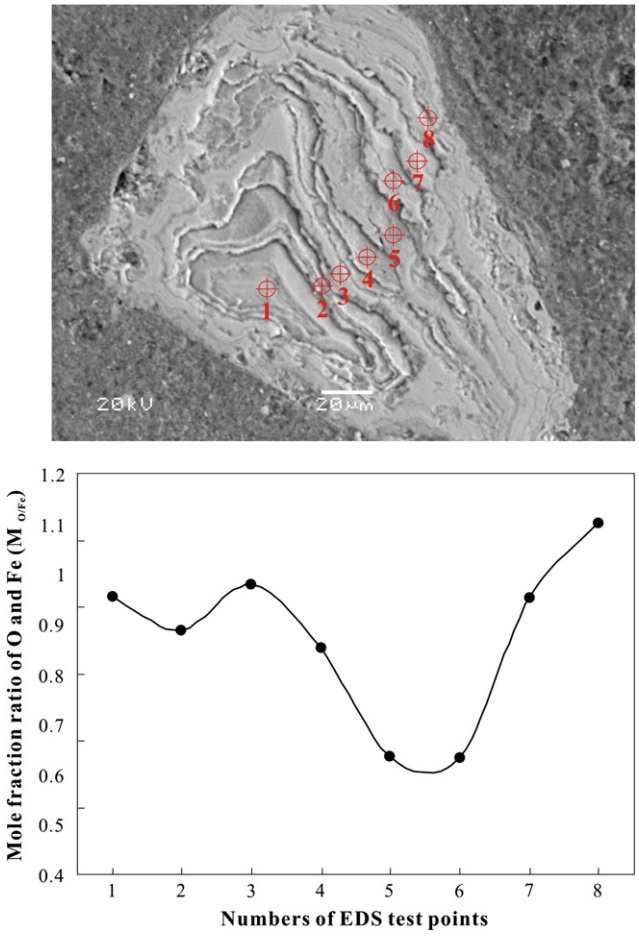

Fig. 12. SEM-EDS image of a small ferruginous concretion within the upper ferruginous nodular horizon of profile XY. (A) Eight EDS points selected on each laminae of the ferruginous concretion. (B) Distribution of mole fraction ratio of O/Fe *vs.* EDS test points.

(5) Typical lateritic weathering covers are generally more concentrated on low hills and karst plains south of the Tropic of Cancer, suggesting that factors such as climate, geomorphology, lithology, and tectonics control the distribution of regolith.
(6) Based on the mineralogical and geochemical investigations, a model for the formation and evolution of typical tropical lateritic profiles was proposed.

Acknowledgments

We appreciate Prof. G.H. Gong and G.F. Zhou for XRD test and EPMA - EDS analytical works, respectively. Moreover, we are grateful to Academician and Prof. C.Q. Liu, and Prof. X.M. Liu, W.J. Lou's discussions and suggestions about this study. This work was jointly supported by the National Natural Science Foundation of China (NSFC) grants (Nos. 41073096 and 40473051), National Key Basic Research Program of China (2013CB956702) and the Hundred Talents Program of the Chinese Academy of Sciences.

References

Abed, A.M., Sadaqah, R.M., 2013. Enrichment of uranium in the uppermost Al-Hisa Phosphorite Formation, Eshidiyya basin, southern Jordan. J. Afr. Earth Sci. 77, 31–40.
Amarasiriwardena, D.D., DeGrave, E., Bowen, L., Weed, S., 1986. Quantitative determination of aluminum-substituted goethite–hematite mixtures by Mössbauer spectroscopy. Clay Clay Miner. 34, 250–256.
Aubert, D., Stille, P., Probst, A., 2001. REE fractionation during granite weathering and removal by waters and suspended loads: Sr and Nd isotopic evidence. Geochim. Cosmochim. Acta 65, 387–406.
Banfield, J.F., Eggleton, R.A., 1990. Analytical transmission electron microscope studies of plagioclase, muscovite, and K-feldspar weathering. Clay Clay Miner. 38, 77–89.
Basu, H., Mahendra Kumar, K., Paneerselvam, S., Chaki, A., 2009. Study of provenance characteristics and depositional history on the basis of U, Th and K abundances in the Gulcheru Formation, Cuddapah Basin in Tummalapalle-Somalollapalle areas, Cuddapah-Anantapur Districts, Andhra Pradesh. J. Geol. Soc. India 74, 318–328.
Beauvais, A., Colin, F., 1993. Formation and transformation processes of iron duricrust systems in tropical humid environment. Chem. Geol. 106, 77–101.
Berner, R.A., Lasaga, A.C., Garrels, R.M., 1983. The carbonate-silicate geochemical cycle and its effect on atmospheric carbon dioxide over the past 100 million years. Am. J. Sci. 283, 641–683.
Boeglin, J.L., Probst, J.L., 1998. Physical and chemical weathering rates and CO_2 consumption in a tropical lateritic environment: the upper Niger basin. Chem. Geol. 148, 137–156.
Braun, J.-J., Pagel, M., Muller, J.-P., Bilong, P., Michard, A., Guillet, B., 1990. Cerium anomalies in lateritic profiles. Geochim. Cosmochim. Acta 54, 781–795.
Braun, J.-J., Viers, J., Dupré, B., Polve, M., Ndam, J., Muller, J.-P., 1998. Solid/liquid REE fractionation in the lateritic system of Goyoum, East Cameroon: the implication for the present dynamics of the soil covers of the humid tropical regions. Geochim. Cosmochim. Acta 62, 273–299.
Braun, J.-J., Marechal, J.-C., Riotte, J., Boeglin, J.-L., Bedimo Bedimo, J.-P., Ndam Ngoupayou, J.R., Nyeck, B., Robain, H., Sekhar, M., Audry, S., Viers, J., 2012. Elemental weathering fluxes and saprolite production rate in a Central African lateritic terrain (Nsimi, South Cameroon). Geochim. Cosmochim. Acta 99, 243–270.
Brimhall, G.H., Dietrich, W.E., 1987. Constitutive mass balance relations between chemical composition, volume, density, porosity, and strain in metasomatic hydrochemical systems: results on weathering and pedogenesis. Geochim. Cosmochim. Acta 51, 567–587.
Buggle, B., Glaser, B., Hambach, U., Gerasimenko, N., Marković, S., 2011. An evaluation of geochemical weathering indices in loess–paleosol studies. Quat. Int. 240, 12–21.
Calagari, A.A., Abedini, A., 2007. Geochemical investigations on Permo-Triassic bauxite horizon at Kanisheeteh, east of Bukan, West-Azarbaidjan, Iran. J. Geochem. Explor. 94, 1–18.
Caspari, T., Baumler, R., Norbu, C., Tshering, K., Baillie, I., 2006. Geochemical investigation of soils developed in different lithologies in Bhutan, Eastern Himalayas. Geoderma 136, 436–458.
Chadwick, O.A., Brimhall, G.H., Hendricks, D.M., 1990. From a black to a gray box—a mass balance interpretation of pedogenesis. Geomorphology 3, 369–390.
Chase, J.W., Winchester, J.W., Coryell, C.D., 1963. Lanthanum, europium and dysprosium distributions in igneous rocks and minerals. J. Geophys. Res. 68, 567–575.
Chen, S., Zhou, F., Luo, D., Wu, Z., Lu, B., Lin, J., 1992. The features and studies on utilizations of the ores of the gibbsite-type bauxite deposits in Guigang, Guangxi. Geol. Guangxi 5, 9–16 (in Chinese with English abstract).
Chen, J., Liu, Y., Xu, J., 1997. The paragenetic deposit of gibbsite and diaspore in western Guangxi. Guangxi Geol. 10, 37–44 (in Chinese with English abstract).
Ching-kuo Daniel, H., Langmuir, D., 1985. Adsorption of uranyl onto ferric oxyhydroxides: application of the surface complexation site-binding model. Geochim. Cosmochim. Acta 49, 1931–1941.
Coleman, N.T., Weed, S.B., McCracken, R.J., 1959. Cation-exchange capacity and exchangeable cations in piedmont soils of North Carolina1. Soil Sci. Soc. Am. J. 23, 146–149.
Compton, J.S., White, R.A., Smith, M., 2003. Rare earth element behavior in soils and salt pan sediments of a semi-aridgranitic terrain in the Western Cape, South Africa. Chem. Geol. 201, 239–255.
Cornell, R.M., 1993. Adsorption of cesium on minerals—a review. J. Radioanal. Nucl. Chem. Artic. 171, 483–500.
Dong, H., Peacor, D.R., Murphy, S.F., 1998. TEM study of progressive alteration of igneous biotite to kaolinite throughout a weathered soil profile. Geochim. Cosmochim. Acta 62, 1881–1887.
Duff, M.C., Amrhein, C., 1996. Uranium(VI) adsorption on goethite and soil in carbonate solutions. Soil Sci. Soc. Am. J. 60, 1393–1400.
Duff, M.C., Hunter, D.B., Triay, I.R., Bertsch, P.M., Reed, D.T., Sutton, S.R., Shea-McCarthy, G., Kitten, J., Eng, P., Chipera, S.J., Vaniman, D.T., 1999. Mineral associations and average oxidation states of sorbed Pu on tuff. Environ. Sci. Technol. 33, 2163–2169.
Duff, M.C., Coughlin, J.U., Hunter, D.B., 2002. Uranium co-precipitation with iron oxide minerals. Geochim. Cosmochim. Acta 66, 3533–3547.
Feng, J.L., 2010. Behaviour of rare earth elements and yttrium in ferromanganese concretions, gibbsite spots, and the surrounding terra rossa over dolomite during chemical weathering. Chem. Geol. 271, 112–132.
Foos, A.M., 1991. Aluminous lateritic soils, Eleuthera, Bahamas; a modern analog to carbonate Paleosols. J. Sediment. Res. 61, 340–348.
Girard, J.-P., Razanadranorosoa, D., Freyssinet, P., 1997. Laser oxygen isotope analysis of weathering goethite from the lateritic profile of Yaou, French Guiana: paleoweathering and paleoclimatic implications. Appl. Geochem. 12, 163–174.
Gong, Q., Deng, J., Yang, L., Zhang, J., Wang, Q., Zhang, G., 2011. Behavior of major and trace elements during weathering of sericite–quartz schist. J. Asian Earth Sci. 42, 1–13.
Gonzalez-Acebron, L., Arribas, J., Mas, R., 2010. Role of sandstone provenance in the diagenetic albitization of feldspars: a case study of the Jurassic Tera Group sandstones (Cameros Basin, NE Spain). Sediment. Geol. 229, 53–63.
Grant, W.H., 1962. Weathering of stone mountain granite. Clay Clay Miner. 11, 65–73.
Halla, J., van Hunen, J., Heilimo, E., Hölttä, P., 2009. Geochemical and numerical constraints on Neoarchean plate tectonics. Precambrian Res. 174, 155–162.
Henderson, P., 1984. General geochemical properties and abundances of the rare earth elements. Rare Earth Elem. Geochem. 2, 1–32.
Horbe, A.M.C., Anand, R.R., 2011. Bauxite on igneous rocks from Amazonia and Southwestern of Australia: implication for weathering process. J. Geochem. Explor. 111, 1–12.
Jeong, G.Y., 2000. The dependence of localized crystallization of halloysite and kaolinite on primary minerals in the weathering profile of granite. Clay Clay Miner. 48, 196–203.

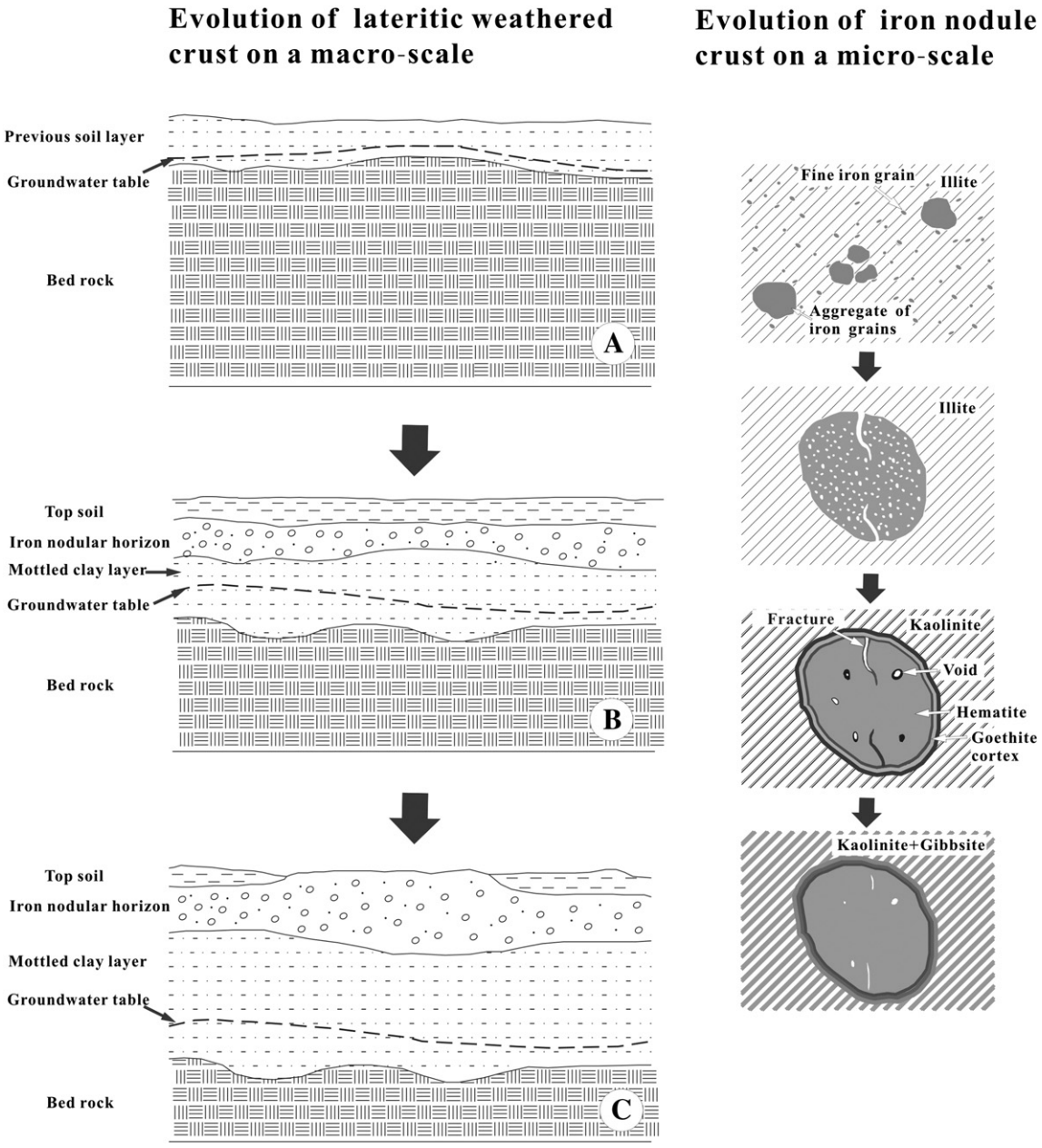

Fig. 13. Model for the formation and evolution of typical lateritic weathering profile in the study area on a macro and micro scale.

Ji, H., Wang, S., Ouyang, Z., Zhang, S., Sun, C., Liu, X., Zhou, D., 2004a. Geochemistry of red residua underlying dolomites in karst terrains of Yunnan-Guizhou Plateau: I. The formation of the Pingba profile. Chem. Geol. 203, 1–27.

Ji, H., Wang, S., Ouyang, Z., Zhang, S., Sun, C., Liu, X., Zhou, D., 2004b. Geochemistry of red residua underlying dolomites in karst terrains of Yunnan-Guizhou Plateau: II. The mobility of rare earth elements during weathering. Chem. Geol. 203, 29–50.

Ji, J., Chen, J., Balsam, W., Lu, H., Sun, Y., Xu, H., 2004c. High resolution hematite/goethite records from Chinese loess sequences for the last glacial–interglacial cycle: rapid climatic response of the East Asian Monsoon to the tropical Pacific. Geophys. Res. Lett. 31, L03207.

Jolicoeur, S., Ildefonse, P., Bouchard, M., 2000. Kaolinite and gibbsite weathering of biotite within saprolites and soils of Central Virginia. Soil Sci. Soc. Am. J. 64, 1118–1129.

Keller, W.D., 1979. Bauxitization of syenite and diabase illustrated in scanning electron micrographs. Econ. Geol. 74, 116–124.

Kretzschmar, R., Robarge, W.P., Amoozegar, A., Vepraskas, M.J., 1997. Biotite alteration to halloysite and kaolinite in soil-saprolite profiles developed from mica schist and granite gneiss. Geoderma 75, 155–170.

Land, M., Ohlander, B., Ingri, J., Thunberg, J., 1999. Solid speciation and fractionation of rare earth elements in a spodosol profile from northern Sweden as revealed by sequential extraction. Chem. Geol. 160, 121–138.

Laskou, M., Margomenou-Leonidopoulou, G., Balek, V., 2006. Thermal characterization of bauxite samples. J. Therm. Anal. Calorim. 84, 141–146.

Laveuf, C., Cornu, S., 2009. A review on the potentiality of rare earth elements to trace pedogenetic processes. Geoderma 154, 1–12.

Li, J., Liu, Z., 2008. Geological characteristics and formation of the gibbsite bauxite deposit in Guangxi, China. Gansu Metall. 30, 56–70 (in Chinese with English abstract).

Liu, C., 1988. The Genetic types of bauxite deposits in China. Sci. Sin. (Ser. B) 31 (8), 1010–1024.

Liu, Y.J., Cao, L., Li, Z., Wang, H., Chu, T., Zhang, J., 1984. Element Geochemistry. Science in China Press.

Liu, X.F., Wang, Q.F., Zhang, Q.Z., Feng, Y.W., Cai, S.H., 2012. Mineralogical characteristics of the superlarge Quaternary bauxite deposits in Jingxi and Debao counties, western Guangxi, China. J. Asian Earth Sci. 52, 53–62.

Lucke, B., Kemnitz, H., Bäumler, R., 2012. Evidence for isovolumetric replacement in some Terra Rossa profiles of northern Jordan. Bol. Soc. Geol. Mex. 64, 21–35.

Ma, Y.J., Huo, R.K., Liu, C.Q., 2002. Speciation and fractionation of rare earth elements in a lateritic profile from southern China: identification of the carriers of Ce anomalies. Geochim. Cosmochim. Acta 66, A471.

Maclean, W.H., 1990. Mass change calculations in altered rock series. Mineral. Deposita 25, 44–49.

MacLean, W.H., Bonavia, F.F., Sanna, G., 1997. Argillite debris converted to bauxite during karst weathering: evidence from immobile element geochemistry at the Olmedo Deposit, Sardinia. Mineral. Deposita 32, 607–616.

Mancktelow, N.S., 1994. On volume change and mass transport during the development of crenulation cleavage. J. Struct. Geol. 16, 1217–1231.

Marques, M.J., Salvador, A., Morales-Rubio, A.E., de la Guardia, M., 2000. Trace element determination in sediments: a comparative study between neutron activation analysis (NAA) and inductively coupled plasma-mass spectrometry (ICP-MS). Microchem. J. 65, 177–187.
Matsuoka, N., 1995. Rock weathering processes and landform development in the Sor-Rondane Mountains, Antarctica. Geomorphology 12, 323–339.
McNeil, M., 1964. Lateritic soils. Sci. Am. 211, 96–102.
Mongelli, G., 1993. REE and other trace elements in a granitic weathering profile from "Serre", southern Italy. Chem. Geol. 103, 17–25.
Murad, E., Schwertmann, U., 1983. The influence of aluminium substitution and crystallinity on the Mössbauer spectra of goethite. Clay Miner. 18, 301–312.
Murad, E., Schwertmann, U., 1986. Influence of Al substitution and crystal size on the room—temperature Mössbauer spectrum of hematite. Clay Clay Miner. 34, 1–6.
Nair, K., Kumar, K., Krishnan, P., Naidu, L., Sarkar, D., 2011. Variability of lateritic soil development in humid tropical environment. Clay Res. 30, 12–20.
Nesbitt, H.W., 1979. Mobility and fractionation of rare-earth elements during weathering of a granodiorite. Nature 279, 206–210.
Nesbitt, H.W., Markovics, G., 1997. Weathering of granodioritic crust, long-term storage of elements in weathering profiles, and petrogenesis of siliciclastic sediments. Geochim. Cosmochim. Acta 61, 1653–1670.
Nesbitt, H.W., Young, G.M., 1982. Early proterozoic climates and plate motions inferred from major element chemistry of lutites. Nature 299, 715–717.
Nesbitt, H.W., Young, G.M., 1984. Prediction of some weathering trends of plutonic and volcanic-rocks based on thermodynamic and kinetic considerations. Geochim. Cosmochim. Acta 48, 1523–1534.
Nesbitt, H.W., Young, G.M., 1989. Formation and diagenesis of weathering profiles. J. Geol. 97, 129–147.
Ng, C.W.W., Guan, P., Shang, Y.J., 2001. Weathering mechanisms and indices of the igneous rocks of Hong Kong. Q. J. Eng. Geol. Hydrogeol. 34, 133–151.
Overstreet, W.C., 1967. The geological occurrence of monazite. US Geol. Surv. Professional Papers 530, 327.
Palumbo, B., Bellanca, A., Neri, R., Roe, M.J., 2001. Trace metal partitioning in Fe–Mn nodules from Sicilian soils, Italy. Chem. Geol. 173, 257–269.
Papoulis, D., Kalampounias, A., 2008. Naturally produced anatase nanostructured films during the hydrothermal alteration of biotite. Proceedings of the IASTED International Confernce Nanotechnology and Applications. NANA, pp. 157–162.
Papoulis, D., Tsolis-Katagas, P., Kalampounias, A.G., Tsikouras, B., 2009. Progressive formation of halloysite from the hydrothermal alteration of biotite and the formation mechanisms of anatase in altered volcanic rocks form Limnos Island, Northeast Aegean Sea, Greece. Clay Clay Miner. 57, 566–577.
Parrish, R.R., 1990. U–Pb dating of monazite and its application to geological problems. Can. J. Earth Sci. 27, 1431–1450.
Rankin, P.C., Childs, C.W., 1976. Rare-earth elements in iron–manganese concretions from some New-Zealand soils. Chem. Geol. 18, 55–64.
Rasmussen, B., Fletcher, I.R., McNaughton, N.J., 2001. Dating low-grade metamorphic events by SHRIMP U–Pb analysis of monazite in shales. Geology 29, 963–966.
Read, D., Bennett, D.G., Hooker, P.J., Ivanovich, M., Longworth, G., Milodowski, A.E., Noy, D.J., 1993. The migration of uranium into peat-rich soils at Broubster, Caithness, Scotland, UK. J. Contam. Hydrol. 13, 291–308.
Rebertus, R.A., Weed, S.B., Buol, S.W., 1986. Transformation of biotite to kaolinite during saprolite-soil weathering. Soil Sci. Soc. Am. J. 50, 810–819.
Rice, C., 1973. Chemical weathering on the Carnmenellis granite. Mineral. Mag. 39, 429–447.
Schaetzl, R., Mikesell, L., Velbel, M., 2006. Soil characteristics related to weathering and pedogenesis across a geomorphic surface of uniform age in Michigan. Phys. Geogr. 27, 170–188.
Schwertmann, U., Fitzpatrick, R.W., Le Roux, J., 1977. Al substitution and different disorder in soil hematites. Clay Clay Miner. 25, 373–374.
Smith, R.E., 1996. Regolith research in support of mineral exploration in Australia. J. Geochem. Explor. 57, 159–173.
Steinmann, M., Stille, P., 1997. Rare earth element behavior and Pb, Sr, Nd isotope systematics in a heavy metal contaminated soil. Appl. Geochem. 12, 607–623.
Sumner, M., Miller, W., Sparks, D., Page, A., Helmke, P., Loeppert, R., Soltanpour, P., Tabatabai, M., Johnston, C., 1996. Cation exchange capacity and exchange coefficients. Methods of soil analysis. Part 3-chemical methods 1201–1229.
Tardy, Y., 1997. Petrology of Laterites and Tropical Soils. AA Balkema.
Tardy, Y., Nahon, D., 1985. Geochemistry of laterites, stability of Al-goethite, Al-hematite, and Fe^{3+} kaolinite in bauxites and ferricretes: an approach to the mechanism of concretion formation. Am. J. Sci. 285, 865–903.
Taylor, S.R., McLennan, S.M., 1985. The continental crust: its composition and evolution. Blackwell Scientific Publication, Oxford 312 pp.
Towell, D.G., Spirn, R.V., Winchester, J.W., 1969. Europium anomalies and the genesis of basalt: a discussion. Chem. Geol. 4, 461–464.
Townsend, F., 1985. Geotechnical characteristics of residual soils. J. Geotech. Eng. 111, 77–94.
Ugolini, F., 1986. Processes and Rates of Weathering in Cold and Polar Desert Environments. Rates of Chemical Weathering of Rocks and Minerals. Academic Press, Inc. 193–235.
Wang, R.H., Li, M., Chen, D.X., 2011. Resource potential prediction for lateritic high-iron gibbsite bauxite deposits in Guangxi. Geol. Bull. China 30, 1303–1311.
Watson, E.B., Harrison, T.M., 1984. Accessory minerals and the geochemical evolution of crustal magmatic systems: a summary and prospectus of experimental approaches. Phys. Earth Planet. Inter. 35, 19–30.
Wells, M.A., Gilkes, R.J., Fitzpatrick, R.W., 2001. Properties and acid dissolution of metal-substituted hematites. Clay Clay Miner. 49, 60–72.
West, G., Dumbleton, M.J., 1970. The mineralogy of tropical weathering illustrated by some west Malaysian soils. Q. J. Eng. Geol. Hydrogeol. 3, 25–40.
White, A.F., Blum, A.E., Schulz, M.S., Bullen, T.D., Harden, J.W., Peterson, M.L., 1996. Chemical weathering rates of a soil chronosequence on granitic alluvium: I. Quantification of mineralogical and surface area changes and calculation of primary silicate reaction rates. Geochim. Cosmochim. Acta 60, 2533–2550.
Wilford, J., 2012. A weathering intensity index for the Australian continent using airborne gamma-ray spectrometry and digital terrain analysis. Geoderma 183–184, 124–142.
Wilford, J., Worrall, L., Minty, B., 2009. Radiometric map of Australia provides new insights into uranium prospectivity. Ausgeo News 95, 1–4.
Wimpenny, J., Gannoun, A., Burton, K.W., Widdowson, M., James, R.H., Gíslason, S.R., 2007. Rhenium and osmium isotope and elemental behaviour accompanying laterite formation in the Deccan region of India. Earth Planet. Sci. Lett. 261, 239–258.
Wronkiewicz, D.J., Condie, K.C., 1987. Geochemistry of Archean shales from the Witwatersrand Supergroup, South Africa: source-area weathering and provenance. Geochim. Cosmochim. Acta 51, 2401–2416.
Xi, C., 1990. Soil condition recording the long term climatic change. Acta Soil Sin. 1, 82–90 (in Chinese with English abstract).
Xing, B.S., Dudas, M.J., 1993. Trace and rare-earth element content of white clay soils of the 3 River Plain, Heilongjiang Province, Peoples-Republic-of-China. Geoderma 58, 181–199.
Yang, W., 1992. A recognition on the relation between Guixian-type bauxization and cenozoic karstification of central Guangxi. Carsologica Sin. 11, 227–239 (in Chinese with English abstract).
Zhao, H., Zhao, X., Hu, S., Ma, H., 2008. Study on the mineralogical characteristics of gibbsite bauxite in China. Conserv. Util. Miner. Resour. 6, 40–44.
Zheng, X., Ge, J., 1983. The discovery and genesis studies of gibbsite from the weathering crust of niobium and tantalum-bearing albitized granite in 414 mining district, Jiangxi Province. Miner. Depos. 1, 87–92 (in Chinese with English abstract).
Zhou, F., Chen, S., 1994. Geochemical characteristics of lateritic weathering crust in Guigang, Guangxi. J. Cent. South Inst. Min. Metall. 25, 151–155 (in Chinese with English abstract).
Zhou, F., Mei, X., 1992. Geological characteristics of Guigang type bauxite deposit. Light Metal (in Chinese with English abstract). 1–7.
Zoller, W.H., Gladney, E.S., Duce, R.A., 1974. Atmospheric concentrations and sources of trace metals at the South Pole. Science 183, 198–200.